

Toward a Consistent Prediction of Defect Chemistry in CeO₂

Xingfan Zhang, Lei Zhu, Qing Hou, Jingcheng Guan, You Lu, Thomas W. Keal, John Buckeridge, C. Richard A. Catlow,* and Alexey A. Sokol*

Cite This: <https://doi.org/10.1021/acs.chemmater.2c03019>

Read Online

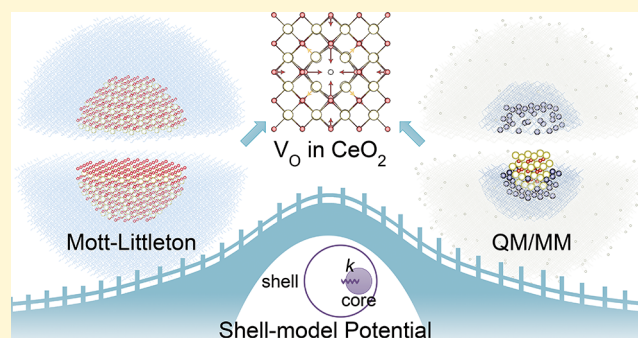
ACCESS |

Metrics & More

Article Recommendations

Supporting Information

ABSTRACT: Polarizable shell-model potentials are widely used for atomic-scale modeling of charged defects in solids using the Mott–Littleton approach and hybrid Quantum Mechanical/Molecular Mechanical (QM/MM) embedded-cluster techniques. However, at the pure MM level of theory, the calculated defect energetics may not satisfy the requirement of quantitative predictions and are limited to only certain charged states. Here, we proposed a novel interatomic potential development scheme that unifies the predictions of all relevant charged defects in CeO₂ based on the Mott–Littleton approach and QM/MM electronic-structure calculations. The predicted formation energies of oxygen vacancies accompanied by different excess electron localization patterns at the MM level of theory reach the accuracy of density functional theory (DFT) calculations using hybrid functionals. The new potential also accurately reproduces a wide range of physical properties of CeO₂, showing excellent agreement with experimental and other computational studies. These findings provide opportunities for accurate large-scale modeling of the partial reduction and nonstoichiometry in CeO₂, as well as a prototype for developing robust interatomic potentials for other defective crystals.



1. INTRODUCTION

Ceria (CeO₂) is a technologically important rare-earth oxide with broad applications in several areas, including heterogeneous catalysis and solid oxide fuel cells (SOFCs).^{1–3} It is versatile in catalytic applications because of its unique defect properties. Apart from its critical role in automobile three-way catalysts, ceria also holds great promise in novel catalytic processes such as selective methane oxidation to methanol, CO₂ conversion reactions, and hydrogen production through water splitting.^{4–6} CeO₂ has outstanding oxygen storage capacity, which arises from its variable stoichiometry enabling the release or uptake of oxygen to pass through redox cycles.⁷ As a consequence, reduced ceria (CeO_{2–x}) is widely used as a supporting material for single-atom/nanocluster catalysts with exceptional catalyst-stabilizing and oxygen-releasing capabilities.^{8–10} In addition, the high ionic conductivity of CeO₂ is necessary for its use as an electrolyte in SOFCs and relies to a large extent on the rapid oxygen-vacancy formation and migration processes.^{11,12} Remarkably, CeO₂ remains very stable in the cubic fluorite structure over a wide range of temperatures. The earth-abundant nature of cerium¹³ further makes it promising for large-scale industrial applications.

Oxygen vacancies are known to have low formation energies in ceria.⁷ Accompanied by the removal of an oxygen ion to form a doubly ionized vacancy V_O^{••}, two excess electrons could localize on two cation sites and form Ce_{Ce}^{••} small polarons^{14,15} or be compensated by an oxygen interstitial O_i[′] to form an

anion–Frenkel pair.¹⁶ Here, we employ the Kröger–Vink notation¹⁷ for a point defect M_S^C, in which M is the defect species, S is the lattice site that the defect occupies, and C is the charge of the defect relative to the original site (dots, primes, and crosses represent positive, negative, and neutral charges, respectively). For the former process, Paier et al.⁷ proposed that the best estimate of the charge-neutral oxygen vacancy formation energy in bulk ceria could be 4.2 ± 0.3 eV (relative to (1/2)E_O) in O-rich conditions deduced from conductivity and calorimetric titration experiments, close to the heat of reduction from CeO₂ to Ce₂O₃ of 4.0 eV.^{18,19} Surface vacancies have much lower (1–3 eV) formation energies than those in the bulk, depending on the facets and concentrations.^{20–24}

In recent years, much effort has been devoted to studying the defect chemistry in CeO₂ by plane-wave density functional theory (DFT) techniques using periodic supercell approaches.^{7,25–31} CeO₂ is a strongly correlated oxide. The description of the highly localized 4f states becomes problem-

Received: October 3, 2022

Revised: November 25, 2022

atic in DFT calculations when Ce^{4+} is reduced to Ce^{3+} . Standard Kohn–Sham DFT calculations using semilocal generalized gradient approximation (GGA) functionals such as Perdew–Burke–Ernzerhof (PBE) predict an unrealistic delocalized spin density for the occupied f states due to the self-interaction error (SIE).²⁵ While the Hubbard U correction scheme³² (DFT+ U , $U_{\text{Ce}4f} = 4.5\text{--}6.0$ eV) can solve the electron localization problem,⁷ the calculated formation energy of the oxygen vacancy (from 2.84 to 3.27 eV^{26–29}) is underestimated by 1.0–1.5 eV compared with experiment (4.2 ± 0.3 eV⁷). Moreover, the choice of the U value is not straightforward, as it introduces uncertainty in the description of bulk properties, defect formation, and surface reactivity of ceria.^{31,33} It has been reported that with the increase in U the lattice constant of CeO_2 becomes too large with increasingly underestimated oxygen vacancy formation energy.³¹ Furthermore, Branda et al.³⁴ reported a variation of the oxidation state of Au on $\text{CeO}_2(111)$ with the U parameter. Watson et al.^{25,26} proposed employing the DFT+ U correction also to the O_{2p} states, which further properly localizes holes in ceria trapped by native defects and impurities. However, this approach underestimates the formation energy of the oxygen vacancy even more: 2.22 eV based on $U_{\text{Ce}/\text{O}} = 5.0/5.5$ eV compared with 2.60 eV using $U_{\text{Ce}/\text{O}} = 5.0/0$ eV. Alternatively, hybrid functionals that include a fraction of the nonlocal Fock exchange, although computationally more demanding, yield results in much closer agreement with experiment. Several hybrid functionals have been used to study the bulk and defect properties of CeO_2 based on periodic models.^{30,31,35–37} Notably, the oxygen vacancy formation energies predicted by hybrid functionals are much closer to experiment than the DFT+ U predictions: 3.84 eV using PBE0³⁸ and 3.63–4.09 eV using HSE06.^{7,30,31} Such improvements from hybrid functionals were also seen in other metal oxide systems with accurately predicted defect processes.³⁹

The configurations of oxygen vacancies and the associated Ce'_{Ce} sites in reduced CeO_2 have been a topic of considerable debate. Early theoretical studies assumed that the two excess electrons are trapped at the nearest neighbor (NN) sites of the vacancy (i.e., NN-NN).^{20,25,40} Later, DFT+ U calculations performed by Wang et al.⁴¹ favored the localization of both electrons at the next-nearest neighbor (NNN) sites (i.e., NNN-NNN). In contrast, Murgida et al.²⁹ obtained three configurations (one NN-NNN and two NNN-NNN configurations) sharing the same lowest formation energies. Despite the minor differences, these predictions are generally consistent. Early molecular-mechanical (MM) Mott–Littleton (M-L) calculations on doped ceria also suggested that large trivalent cations prefer to locate at the NNN sites over the NN sites.⁴² Scanning-tunneling microscopy (STM) imaging over the $\text{CeO}_2(111)$ surface conducted by Jerratsch et al.⁴³ captured several different configurations, indicating that at least one Ce'_{Ce} is not adjacent to the vacancy site. The polarization energy of $\text{V}_\text{O}^{\bullet\bullet}$ is large due to the high dielectric constants of CeO_2 , which can stabilize isolated charged species with respect to the neutral lattice, including both $\text{V}_\text{O}^{\bullet\bullet}$ and Ce'_{Ce} . Besides, the formation of Ce'_{Ce} requires an expansion of the surrounding lattice, which opposes the location next to the oxygen vacancy site where the neighboring Ce–O bonds shrink. As a result, the binding energy of $\text{V}_\text{O}^{\bullet\bullet}$ with the NN Ce'_{Ce} polaron is very low (ca. 0.1 eV as reported by Sun et al.³⁰), indicating that Ce'_{Ce} polarons are not tightly bound to oxygen vacancies. Experimentally, early conductivity measurements by Tuller

and Nowick⁴⁴ on single-crystal CeO_{2-x} samples also revealed that $\text{V}_\text{O}^{\bullet\bullet}$ is the predominant charge state at a small x in CeO_{2-x} ($x < 10^{-3}$), with a transition to singly ionized $\text{V}_\text{O}^\bullet$ at a larger x in more reducing environments. In addition, a recent cathodoluminescence spectroscopy study by Thajudheen et al.⁴⁵ demonstrated that the relative concentration of different charge states of oxygen vacancies depends on the oxygen partial pressure. Luo et al.¹⁶ observed using neutron scattering that the anion–Frenkel pair is dominant in the bulk, while Ce'_{Ce} polarons tend to aggregate at the surface and form an ordered reduced phase from nanorod samples. Such complexity in the charge compensation mechanism of oxygen vacancies could have a substantial impact on the ionic conductivity in SOFCs¹² and surface reactivity when CeO_2 serves as a catalyst⁴⁶ or support.⁴⁷ To resolve these uncertainties, reliable theoretical techniques are required to study the environmentally dependent formation mechanisms of all the relevant charge states of intrinsic defects in CeO_2 .

While being well-suited to modeling bulk materials and delocalized states, periodic boundary conditions have inherent limitations in modeling localized states such as isolated defects, polarons, and adsorbed molecules due to spurious image–image interactions. The long-range Coulomb interactions between periodic images originating from the net dipole moment of localized states are non-negligible.⁴⁸ As a result, periodic DFT calculations on defective solids usually require a large supercell to mitigate these spurious periodic interactions,^{7,29} and additional correction schemes are usually necessary to achieve a higher level of accuracy.^{48–50} Also, for some highly charged defects, the finite-size supercells could still be insufficient to fully consider the long-range atomic perturbations. In particular, the formation of highly charged defects in CeO_2 , such as $\text{Ce}_i^{\bullet\bullet\bullet}$ and $\text{V}_{\text{Ce}}^{\bullet\bullet\bullet}$, could provide a major perturbation of the surrounding atomic structure. These errors could be magnified when defect clusters are considered. Additionally, it is computationally very demanding with hybrid functionals to employ a sufficiently large supercell to minimize these errors.

A minor change in the formation energy of a point defect could result in several orders of magnitude variations in its calculated concentration, which could strongly affect the predicted electronic and optical properties.³⁹ Therefore, minimizing errors in the modeling method is necessary to ensure the accuracy of defect predictions. Embedded-cluster techniques that naturally avoid periodic image interactions and further consider long-range polarization effects are an effective approach to modeling localized defects in solids at the dilute limit.^{51–56} The Molecular Mechanical, Mott–Littleton (MM M-L) approach^{57–59} and hybrid quantum mechanical/molecular mechanical (QM/MM) embedded-cluster techniques^{55,60,61} are widely used for modeling defect processes in solids. Both methods are based on the embedded-cluster framework: the QM/MM model includes a QM core, an interface, and part of MM atoms in the active region, while the M-L model only has one active MM region, which is allowed to relax fully in response to the formation of charged defects; the outer fixed part reproduces the infinite bulk environment.⁵⁹ The M-L approach treats the outer part within a harmonic approximation to reproduce the bulk crystal field and linear dielectric response, while our QM/MM model implements a simplified continuous dielectric medium approximation where the response to the defect charge is calculated *a posteriori*.⁵⁵ Furthermore, the shell-model⁶² interatomic potential (IP) is

	a_0 (Å)	Z_{Ce}^*	Z_O^*	C_{11} (GPa)	C_{12} (GPa)	C_{44} (GPa)	B_0 (GPa)	ϵ_0	ϵ_∞	$F_{1u}(TO)(cm^{-1})$	$F_{2g}(cm^{-1})$	$F_{1u}(LO)(cm^{-1})$	ΔU_L (eV)	E_{ig}^* (eV)	E_{og}^* (eV)	$E_{V_O}^{**}$ (eV)	E_{Ce}^{***} (eV)	$E_{cation-Frenkel}$ (eV)	$E_{anion-Frenkel}$ (eV)	$E_{Schottky}$ (eV)	$E_{interstitial}$ (eV)	$E_{O_{100}}^{surf}$ (eV)	$E_{O_{110}}^{surf}$ (Jm ⁻²)	$E_{O_{111}}^{surf}$ (Jm ⁻²)	E_{IP10a}^{surf} (Jm ⁻²)	E_{IP10b}^{surf} (Jm ⁻²)
IP1	-5.468	5.80	-2.90	490.2	140.6	132.4	257.1	22.52	5.41	301.4	509.9	614.6	-104.6	15.60	-10.42	83.53	-64.28	9.63	2.59	3.37	6.50	N/A	3.13	1.22	1.08	
IP2	-5.411	5.44	-2.72	504.4	143.1	16.2	263.5	19.45	4.00	302.1	518.6	666.4	-105.6	15.99	-10.48	83.39	-66.29	8.55	2.75	3.24	6.13	0.73	2.04	1.60	1.22	
IP3	-5.382	4.76	-2.38	534.7	137.7	73.9	270.0	17.06	1.94	269.3	529.7	799.6	-106.3	15.88	-9.67	85.41	-64.83	10.29	3.11	3.62	7.39	0.58	2.63	2.10	1.38	
IP4	-5.410	3.33	-1.66	554.5	124.6	123.4	267.9	18.58	4.54	193.9	325.4	392.3	-105.7	15.39	-9.00	85.43	-63.22	11.10	3.20	3.52	8.14	0.30	2.91	2.14	1.36	
IP5	-5.410	3.10	-1.55	573.0	147.8	146.8	289.5	12.69	3.98	229.6	341.2	410.0	-106.7	16.52	-9.24	87.73	-62.19	12.77	3.64	4.69	8.68	0.58	3.55	2.44	1.56	
IP6	-5.410	3.06	-1.53	554.5	124.6	123.1	267.9	18.62	5.88	187.2	283.4	333.2	-105.7	15.39	-9.00	85.42	-63.23	11.09	3.20	3.52	8.14	0.30	2.90	2.14	1.36	
IP7	-5.426	4.49	-2.25	470.9	99.3	62.9	223.2	20.00	4.76	250.3	425.4	512.9	-103.0	15.14	-8.94	80.22	-63.87	8.18	3.10	2.49	7.09	N/A	1.32	1.83	1.06	
IP8	-5.407	4.07	-2.04	405.5	104.3	60.6	204.7	18.71	4.01	232.2	431.7	501.4	-101.9	16.71	-11.88	76.81	-57.80	9.50	2.41	2.77	6.78	0.31	1.94	2.17	1.38	
IP9	-5.411	5.49	-2.74	405.3	109.2	64.4	207.9	24.22	5.31	275.5	473.3	588.3	-102.9	12.91	-6.52	94.41	-62.53	15.94	3.20	5.79	9.10	0.55	5.19	4.80	3.62	
IP10a	-5.395	5.68	-2.84	526.9	138.7	59.5	268.1	24.52	5.27	283.9	484.8	612.3	-106.0	15.43	-9.90	84.37	-66.76	8.74	2.75	3.07	6.42	0.55	2.40	1.57	1.18	
IP10b	-5.395	5.45	-2.72	404.2	115.8	60.7	211.9	24.50	5.31	272.8	465.3	585.8	-107.5	16.02	-11.72	85.23	-67.99	8.62	2.15	3.25	5.36	0.53	2.54	1.41	0.74	
Expt. / PBE0	-5.395	5.67	-2.84	403.0	105.0	60.0	220.0	24.50	5.31	273.0	465.0	597.0		16.19	-11.71	84.62	-67.67	8.48	2.25	3.08	5.56	0.52	1.61	1.21	0.85	

Figure 1. Performance of the previous (IP1-IP9) and our newly developed (*IP10a* and *IP10b*) shell-model potentials for modeling CeO₂, compared with experimental and first-principles results. *IP10a* is developed based on the pure Buckingham potential in short-range interactions, while *IP10b* is the refined final version with improved performance, using a more complex potential form. The calculated values of each observable based on the corresponding potential are shown in the blocks. The blocks are colored according to the relative errors of the predicted properties compared with these experimental or theoretical references. Lattice constant a_0 (extrapolated to 0 K),^{33,81} elastic constants C_{11} , C_{12} , and C_{44} ,⁸² phonon frequencies $F_{1u}(TO)$, F_{2g} , and $F_{1u}(LO)$,⁸² static and high-frequency dielectric constants ϵ_0 and ϵ_∞ ,⁸³ bulk modulus B_0 ,⁸⁴ and migration barrier of oxygen vacancy $E_{V_O}^{migration}$ ⁸⁵ are from previous experiments. References for Born effective charges Z_{Ce}^* and Z_O^* and surface energies $E_{(100)}^{surf}$, $E_{(110)}^{surf}$, and $E_{(111)}^{surf}$ are calculated at the PBE0 level of theory using VASP. References for the defect energies including $E_{V_O}^{**}$, E_{O}^* , $E_{V_{Ce}}^{***}$ and E_{Ce}^{***} and defect pair/trio formation energies $E_{cation-Frenkel}$, $E_{anion-Frenkel}$, $E_{Schottky}$, and $E_{interstitial}$ are calculated based on our hybrid QM/MM embedded-cluster model at the PBE0 level.

typically used in both techniques, in which the contributions of electronic long-range polarization effects due to the defect formation to the total energy can be computed through shell relaxations. With the rapid development of high-performance computing platforms, embedded-cluster calculations routinely employ over one thousand or more atoms in the active region (including QM and MM atoms) to consider explicitly the atomic displacements caused by defects, ensuring accuracy in predicting the formation energies and spectroscopic features.^{54,63}

M-L calculations of defects in solids are performed at the pure MM level, which relies heavily on the accuracy of the IP. A reliable shell-model IP is a fundamental prerequisite for quantitatively predicting the defect structures and formation energies. In contrast, embedded-cluster results commonly use DFT calculations employing hybrid functionals (although higher level theory may be used⁶⁴⁻⁶⁶) and with the IP-predicted dielectric response. Hence, an intrinsically consistent prediction of defect structures and formation energies by both approaches using the same potential is the ultimate goal that demonstrates the robustness of an IP. In previous work, such consistent predictions were achieved for MgO^{67,68} and ZnO^{51,69} but were limited to a few charge states of point defects without holes or electrons.

To date, a number of shell-model potentials have been developed for CeO₂, which are collected in Table S1.^{42,70-76} IP-based computational studies of defect chemistry in ceria were first performed by Butler, Catlow, Cormack et al.^{70,77,78} using the M-L approach; these studies calculated vacancy

migration energies in good agreement with experiment and demonstrated the crucial role of the ionic radius of dopants in determining the solution energy and the magnitude of dopant-vacancy interactions. Periodic models were also exploited to investigate the oxygen vacancy formation on surfaces and its role in CO oxidation.^{71,79,80} Despite these advances, no single IP can offer a consistently accurate description of all the physical and chemical properties of CeO₂, as shown in Figure 1. It was possible to reproduce accurately the main bulk properties of ceria, including phonon frequencies and the oxygen vacancy migration barrier based on a more complex potential model (IP9 in Table S1),⁷⁶ but the defect formation and surface energies proved to be significantly overestimated. One of the critical reasons for the less satisfying performance of previous potentials is the lack of reliable reference data in the IP development that exacerbates the errors in empirical parametrization.

In this work, we propose a novel methodology for IP development assisted by the QM/MM approach, which allows us to obtain accurate reference data for ionic polarizabilities, structure and formation energies of polarons, and intrinsic defects in dielectric materials. A new shell-model IP has been developed for CeO₂ that reproduces accurately the experimental structure, elastic and dielectric constants, defect and surface properties, and phonon dispersion. This approach also provides references for parametrizing localized holes and polarons, endowing powerful capacities for modeling the localization of charge carriers accompanied by defect formation. Based on the new IP, the calculated structure and

formation energies of charged defects by the M-L and QM/MM approaches using hybrid functionals achieve a very high level of consistency, which is greater than that achieved in previous work. Our potential is parametrized entirely using the shell-model and pairwise potentials without complex many-body interactions, ensuring excellent computational efficiencies in studying complex defective systems. Moreover, the newly proposed strategies for developing reliable shell-model potentials for accurate defect predictions assisted by QM/MM calculations could be extended to other systems.

2. METHODOLOGY

This work combines various computational techniques including plane-wave DFT calculations, IP-based lattice and M-L defect calculations, and the hybrid QM/MM embedded-cluster approach.

2.1. Plane-Wave DFT Calculations. Plane-wave DFT calculations were performed at several levels of theory using the Vienna Ab-initio Simulation Package (VASP)⁸⁶ to set theoretical references for developing new IPs. Full computational details for calculating the bulk and surface properties of ceria are given in Section S1.1 of the Supporting Information.

2.2. Interatomic-Potential-Based Calculations. The development of IPs and IP-based calculations are performed based on the Born model of ionic solids⁸⁷ using the General Utility Lattice Package (GULP) code.^{88,89} In traditional shell-model potentials, pairwise interactions are described by the Buckingham potential:

$$V_{ij}(r_{ij})^{\text{Buckingham}} = A \exp\left(-\frac{r_{ij}}{\rho}\right) - C_{\delta} r_{ij}^{-6} \quad (1)$$

where r_{ij} is the distance between two interacting ions and A , ρ , and C_{δ} are the parameters. Ionic polarizability is treated by the shell model, in which the massless shell is connected to the atomic core by a harmonic spring with a spring constant k_2 :

$$E_{\text{sm}} = \frac{1}{2} k_2 (\delta r_i)^2 \quad (2)$$

The sum of the core and shell charges on an ion equals its formal charge. The ionic polarizability α in vacuum in the shell model is given by

$$\alpha = \frac{Y^2}{k_2} \quad (3)$$

where Y is the shell charge. The electrostatic Coulomb interaction is calculated as

$$V_{ij}(r_{ij})^{\text{Coulomb}} = \frac{k_e q_i q_j}{r_{ij}} \quad (4)$$

where k_e is the dimensional Coulomb constant ($14.3996 \text{ eV } \text{\AA}^{-2}$).

In this work, our new potential keeps the classical Buckingham form for describing the O–O and Ce–Ce interactions, while taking a complex form combining repulsive and attractive terms for Ce–O interactions parametrized in GULP. This potential can be represented by using the Buckingham, 12-6 Lennard-Jones, Morse-like, and constant offset (0-order polynomial) analytical forms in GULP:

$$V_{ij}(r_{ij}) = A \exp\left(-\frac{r_{ij}}{\rho}\right) - C_{\delta} r_{ij}^{-6} + \frac{E}{r_{ij}^{12}} + D[(1 - \exp(-a(r_{ij} - r_0)))^2 - 1] + c_0 \quad (5)$$

where A , ρ , C_{δ} , E , D , a , r_0 , and c_0 are the parameters of the potential.

IP-based defect calculations were undertaken based on the M-L approach.^{57,58} A point defect or defect cluster is embedded in the central part of the model (region I), where ionic relaxations and polarization are allowed explicitly. The surrounding regions (region IIa and IIb) that model the infinite solid are described within the linear response approximation. Region IIa acts as the interface, in

which interactions with region I ions are calculated by explicit summation, but ionic displacements are calculated self-consistently using a harmonic approximation for the defect energy expanded around defect equilibrium configuration, as first proposed by Norgett⁹⁰ and implemented in the GULP code.⁸⁸ Region IIb extends to infinity to reproduce the periodic electrostatic environment of the solid, in which the long-range polarization energy of a charged defect outside the active region I is calculated using the macroscopic dielectric response of a perfect crystal (without a defect). The radii of region I and region IIa were set to 25 Å and 40 Å, respectively, which proved to be sufficiently large for considering the long-range polarization effects and provide well-converged defect energies (<0.1 eV).

Details of IP-based surface and vacancy migration calculations are described in Sections S1.2 and S1.3 of the Supporting Information.

2.3. QM/MM Calculations. We employ the hybrid QM/MM embedded-cluster approach to model defect formation in bulk CeO₂ as implemented in the ChemShell^{60,91} code. Our hybrid QM/MM embedded-cluster model is divided into five regions. In the QM region, electronic-structure calculations are performed at the hybrid DFT level using NWChem.⁹² We have tested the performance of several pseudopotentials and basis sets to balance the computational accuracy and efficiency in large-scale QM/MM calculations of CeO₂ (with 100–200 QM atoms). The combination of the Def2-TZVP basis set⁹³ for O and a [4s4p2d3f] basis set developed by Erba et al.^{94,95} based on the Stuttgart–Dresden quasi-relativistic small-core (28 core electrons) effective core potential (ECP)⁹⁶ for Ce was determined as the best choice. The differences in the calculated formation energies of defects and ionization potential between the current setting and more complete basis sets are less than 0.1 eV. We utilized three hybrid functionals for defect calculations: hybrid GGA functional B97-2⁹⁷ and PBE0⁹⁸ and hybrid meta-GGA functional BBIK,⁹⁹ which include 21%, 25%, and 42% HF exact exchange, respectively. For consistency, we selected PBE0 results as the reference data in the IP development, together with those from VASP calculations using the same functional.

The MM calculations are performed using GULP. The MM part of the QM/MM structural model is divided into two regions: the MM-active region, which is allowed to relax during the calculations, and the MM-frozen region, which is fixed to reproduce the effect of the bulk environment. The outermost layer of the entire model includes point charges, which were fitted to eliminate the effects of surface termination and reproduce the Madelung potential of CeO₂.

The interface region participates in both QM and MM interactions, serving as the buffer layer to minimize the mismatch of the QM and MM levels of theory. We used a specially designed local pseudopotential on the cationic sites in the form of a linear combination of three Gaussian functions.⁵⁶ The fundamental idea and detailed procedures of the QM/MM interface treatment are shown in Section S1.4 of the Supporting Information. The parameters were trained with a least mean square procedure for residual gradients on the ions in the active (QM, interface, and MM-active) region and the scatter of deep core levels (in this study, O_{1s}) in the Kohn–Sham spectrum. The fitted pseudopotential for the interface cations has the form of

$$U_p(r) = \frac{1}{r^2} (-49.817re^{-24.9589r^2} + 60.247r^2e^{-2.85901r^2} + 0.295877r^2e^{-0.25855r^2}) \quad (6)$$

QM/MM defect calculations were performed with the python-based version of ChemShell (Py-ChemShell)⁹¹ on a large embedded-cluster model with ~10 000 atoms in total and an O-centered 197-atom QM cluster focusing on the formation of oxygen vacancies. The accurately calculated energies of polaron formation at the NN and NNN sites have been used for validation and refinement of the interatomic potentials that we report. A Ce-centered 111 QM-atom model was used for other types of defects, which yields convergence of defect formation energies to ca. 0.1 eV.

2.4. Calculations of Defect Formation Energies. Lattice energy is the energy of the ionic compound with respect to constituent ions in the gas phase. The lattice energy ΔU_L can be calculated according to the Born–Haber cycle¹⁰⁰ from experimental thermodynamical data, which (for CeO₂) is given by

$$\Delta U_L = \Delta H_{\text{subl}}(\text{Ce}) + D_{\text{O}_2} + I_{\text{Ce}}^{1-4} + A_{\text{O}}^{1-2} - \Delta H_f(\text{CeO}_2) \quad (7)$$

where $\Delta H_{\text{subl}}(\text{Ce})$ is the sublimation enthalpy of Ce (4.380 eV¹⁰¹), D_{O_2} is the dissociation energy of O₂ (5.136 eV¹⁰¹), I_{Ce}^{1-4} is the sum of the first four ionization potentials of Ce (73.745 eV¹⁰¹), A_{O}^{1-2} is the sum of the first (A_{O}^1) and second (A_{O}^2) electron affinities of O, and $\Delta H_f(\text{CeO}_2)$ is the formation enthalpy of CeO₂ (−11.28 eV¹⁰¹). While A_{O}^1 is experimentally known as 1.461 eV,¹⁰² A_{O}^2 is dependent on the atomic environment of oxides, adding uncertainty to the IP development and subsequent defect formation calculations. Freeman and Catlow suggested a value of 8.75 eV for SnO₂, while Waddington¹⁰³ obtained an average value of 9.41 eV from several oxides. Previous work has shown that ΔU_L is a critical quantity that strongly affects the accuracy of M-L defect calculations.¹⁰⁴ However, fitting the potential to reproduce the “experimental” ΔU_L according to an arbitrary choice of A_{O}^2 may be problematic and could lead to several electronvolt errors in the calculated formation energies. We propose a self-consistent approach to determine the value of A_{O}^2 in CeO₂ (8.14 eV, and therefore $\Delta U_L = -107.5$ eV according to eq 7) based on QM/MM calculations of defect energies and plane-wave DFT calculations of surface energies, which will be discussed in the following sections. For the defect formation energy calculations using the Born–Haber cycle based on the M-L results, a consistent usage of the A_{O}^2 and ΔU_L predicted by the IP gives accurate results that are comparable with QM/MM calculations.

It is necessary to clarify the definition of some energy terms in defect calculations. In QM/MM calculations, the formation energy of a defect in the charge state of q is defined as

$$E_f[X^q] = E[X^q] - E_0 - \sum_i n_i \mu_i + qE_F + E_{\text{corr}} \quad (8)$$

where $E[X^q]$ and E_0 are the calculated total QM/MM energies of the defect and perfect structures, n_i is the number of species that have been added ($n_i > 0$) or removed ($n_i < 0$) from the system to form the defect, μ_i is the chemical potential of the species i , and E_F is the Fermi level relative to the valence band maximum (VBM). In order to account for the long-range polarization effect for charged defects that extends to infinity, an *a posteriori* correction is applied using the Jost formula,^{61,105}

$$E_{\text{corr}} = -\frac{Q^2}{2R} \left(1 - \frac{1}{\epsilon}\right) \quad (9)$$

where R is the radius of the active region (including QM, interface, and MM-active regions) and Q is the net charge of the defect system. High frequency ϵ_∞ and static ϵ_0 dielectric constants are used for vertical and adiabatic processes, respectively.

M-L calculations compute the defect energy $E[X^q]$ taking the gas phase ions (O^{2−}(g) and Ce⁴⁺(g)) as the reference, which differs from the formation energy (with respect to O₂(g) and Ce(s)) in conventional DFT calculations. The energy of O₂(g) and Ce(s) is not defined in IP-based calculations. Instead, such energies can be in turn obtained from the Born–Haber cycle¹⁰⁰ and relate $E[X^q]$ to $E_f[X^q]$ by

$$\frac{1}{2}\text{O}_2(\text{g}) \rightarrow \text{O}(\text{g}) \rightarrow \text{O}^{2-}(\text{g}) - 2e^- \quad (10)$$

$$\text{Ce}(\text{s}) \rightarrow \text{Ce}(\text{g}) \rightarrow \text{Ce}^{4+}(\text{g}) + 4e^- \quad (11)$$

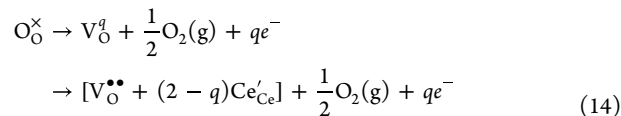
Therefore, the energy of the added or subtracted species in defect formation can be obtained by

$$E_{1/2\text{O}_2(\text{g})} = E_{\text{O}^{2-}(\text{g})} - A_{\text{O}}^{1-2} - \frac{1}{2}D_{\text{O}_2} \quad (12)$$

$$E_{\text{Ce}(\text{s})} = E_{\text{Ce}^{4+}(\text{g})} - I_{\text{Ce}}^{1-4} - \Delta H_{\text{subl}}(\text{Ce}) \quad (13)$$

Accordingly, the defect energies $E_{\text{V}_\text{O}}^{\bullet\bullet}$, $E_{\text{O}_\text{O}}^{\prime}$, $E_{\text{V}_\text{Ce}}^{\prime\prime}$, and $E_{\text{Ce}_\text{Ce}}^{\prime\prime\prime}$ can be directly obtained and compared in M-L and QM/MM approaches. Furthermore, the energy changes during the formation of localized electrons or holes trapped by the defects do not include the fourth ionization potential of Ce (I_{Ce}^4 , 36.762 eV¹⁰¹) or A_{O}^2 , which should be subtracted from the M-L-calculated defect energies.¹⁰⁰ Defect energies calculated by the M-L approach implemented in GULP have already accounted for the long-range polarization effect, so extra corrections are not needed.

For example, when an oxygen vacancy V_O^q with a charge state q ($q = 0, +1, +2$) is formed in CeO₂, the excess $2 - q$ electrons are not trapped at the vacancy site but will localize on the nearby Ce site to form Ce_{Ce}^q small polarons. This process can be formed thus:



The formation energy determined using M-L calculations is then calculated as the corresponding reaction energy:

$$\begin{aligned} E_f[\text{V}_\text{O}^q] &= E[\text{V}_\text{O}^{\bullet\bullet} + (2 - q)\text{Ce}'_{\text{Ce}}] - A_{\text{O}}^{1-2} - \frac{1}{2}D_{\text{O}_2} \\ &\quad - (2 - q)I_{\text{Ce}}^4 + \mu_\text{O} + qE_F \end{aligned} \quad (15)$$

where $E[\text{V}_\text{O}^q] = E[\text{V}_\text{O}^{\bullet\bullet} + (2 - q)\text{Ce}'_{\text{Ce}}]$ is the defect energy obtained from an M-L calculation and E_F is the Fermi level relative to VBM. Similarly, a cerium vacancy with a charge state q ($q = 0, -1, -2, -3, -4$) can trap $(4 + q)$ localized holes O_O^q. The formation energy of V_{Ce}^q can be calculated by

$$\begin{aligned} E_f[\text{V}_{\text{Ce}}^q] &= E[\text{V}_{\text{Ce}}^{\prime\prime\prime} + (4 + q)\text{O}_\text{O}^q] - I_{\text{Ce}}^{1-4} - \Delta H_{\text{subl}}(\text{Ce}) \\ &\quad - (4 + q)A_{\text{O}}^2 + \mu_{\text{Ce}} + qE_F \end{aligned} \quad (16)$$

Also, the formation energies of oxygen interstitials $E_f[\text{O}_\text{O}^q]$ are calculated by

$$\begin{aligned} E_f[\text{O}_\text{O}^q] &= E[\text{O}_\text{O}^{\prime} + (2 + q)\text{O}_\text{O}^q] + A_{\text{O}}^{1-2} + \frac{1}{2}D_{\text{O}_2} - (2 + q)A_{\text{O}}^2 \\ &\quad - \mu_\text{O} + qE_F \end{aligned} \quad (17)$$

Finally, the formation energies of cerium interstitials $E_f[\text{Ce}'_{\text{Ce}}]$ are calculated by

$$\begin{aligned} E_f[\text{Ce}'_{\text{Ce}}] &= E[\text{Ce}_\text{Ce}^{\prime\prime\prime} + (4 - q)\text{Ce}'_{\text{Ce}}] + I_{\text{Ce}}^{1-4} + \Delta H_{\text{subl}}(\text{Ce}) \\ &\quad - (4 - q)I_{\text{Ce}}^4 - \mu_{\text{Ce}} + qE_F \end{aligned} \quad (18)$$

The formation energy of a charged defect is also dependent on the growth conditions. In the O-rich/Ce-poor conditions, the upper limit is determined by the formation of O₂ molecules, in which $\mu_\text{O} = 0$ eV and $\mu_{\text{Ce}} = \Delta H_f(\text{CeO}_2)$. In O-poor/Ce-rich conditions, the lower limit of μ_O is determined not only by CeO₂ but also by other Ce_{*n*}O_{*m*} phases, where CeO₂ should remain more stable than any other reduced phases. Conventionally, we take Ce₂O₃ as the limiting phase as employed in previous DFT calculations.^{27,28,30} Hence,

$$\mu_{\text{Ce}} + 2\mu_\text{O} = \Delta H_f(\text{CeO}_2) \quad (19)$$

$$2\mu_{\text{Ce}} + 3\mu_\text{O} < \Delta H_f(\text{Ce}_2\text{O}_3) \quad (20)$$

Therefore, the chemical potentials should satisfy

$$\mu_\text{O} > 2\Delta H_f(\text{CeO}_2) - \Delta H_f(\text{Ce}_2\text{O}_3) \quad (21)$$

$$\mu_{\text{Ce}} < 2\Delta H_f(\text{Ce}_2\text{O}_3) - 3\Delta H_f(\text{CeO}_2) \quad (22)$$

Thermochemical experimental measurements give $\Delta H_f(\text{CeO}_2) = -11.28$ eV and $\Delta H_f(\text{Ce}_2\text{O}_3) = -18.62$ eV,¹⁰¹ which allows us to

Table 1. Calculated Lattice Constant a_0 , Band Gap E_g , High-Frequency Dielectric Constant ϵ_∞ , Born Effective Charges Z_{Ce}^* and Z_{O}^* , and Surface Energies of CeO_2 Using VASP Compared with Previous Experimental and Theoretical Results

	a_0 (Å)	E_g (eV)	ϵ_∞	Z_{Ce}^*	Z_{O}^*	$E_{(100)}^{\text{surf}}$ (J m ⁻²)	$E_{(110)}^{\text{surf}}$ (J m ⁻²)	$E_{(111)}^{\text{surf}}$ (J m ⁻²)
PBE+U ($U_{\text{Ce } 4f} = 5$ eV) ^a	5.490	2.29	6.59	5.53	-2.77	1.45	1.06	0.69
PBEsol+U ($U_{\text{Ce } 4f} = 5$ eV) ^a	5.435	2.41	6.57	5.51	-2.75	1.77	1.27	0.90
PBE0 ^a	5.397	4.38	5.67	5.67	-2.84	1.61	1.21	0.85
PBEsol0 ^a	5.361	4.46	5.68	5.68	-2.84	1.83	1.33	0.96
HSE06 ^a	5.396	3.63	5.71	5.67	-2.84	1.59	1.20	0.84
PBE+U ($U_{\text{Ce } 4f} = 5$ eV) ^b	5.489					1.44	1.06	0.71
PBEsol+U ($U_{\text{Ce } 4f} = 5$ eV) ^c	5.431		6.55	5.53	-2.76			
PBE0 ^d	5.403	4.35						
PBE0 ^e	5.401					1.64	1.27	0.86
PBEsol0 ^d	5.368	4.40						
HSE06 ^f	5.40	3.50						
GW0 ^g		3.88						
Experiment	5.411 ^h	2.9–3.3 ^k	5.31 ^q			1.20 ± 0.2 (averaged) ^r		
	5.401 ⁱ	4.0 ^l						
	5.395 ^j	3.6–4.11 ^m						
		4.0 ⁿ						
		4.4 ^o						
		4.3–4.4 ^p						

^aPresent work. ^bReference 121. ^cReference 122. ^dReference 37. ^eReference 38. ^fReference 35. ^gReference 123. ^hRoom-temperature measurements.^{108–110} ⁱLow-temperature measurement at 100 K.¹¹³ ^jExtrapolated to 0 K from thermal expansion measurements.^{81,111–113} ^kSpectroscopic ellipsometry measurement on nanocrystalline or single-crystal CeO_{2-x} films.^{106,116} ^lSteady-state and ultrafast transient absorption spectra measurement on stoichiometric CeO_2 thin film. A revised optical band gap of 4 eV was proposed for bulk ceria, and the absorption tail below 4 eV was identified as the Urbach tail.¹¹⁷ ^mOptical measurement on polycrystalline CeO_2 films with 140–180 nm thicknesses.¹²⁴ ⁿThe electron energy loss spectroscopy (EELS) spectrum captured the $\text{O}_{2p} \rightarrow \text{Ce}_{4f}$ transition starting at 4 eV on single-crystal thin films, and the intensity between 0 and 3 eV indicates the Ce^{3+} state.¹²⁰ ^oHigh-resolution EELS study on stoichiometric thin films observed a 4.4 eV energy loss from O_{2p} to the empty Ce_{4f} state transition.¹¹⁹ ^pMeasurement from the optical absorption spectrum on the CeO_2 nanoparticles.¹¹⁸ ^qTransmissivity and reflectivity measurement on CeO_2 quasi-single crystal sample.⁸³ ^rMeasurement on nanoparticle samples by calorimetry methods.^{125,126}

calculate $\mu_{\text{O min}} = -3.94$ eV and $\mu_{\text{Ce max}} = -3.40$ eV, which were used in our calculations. In QM/MM calculations, the reference energies for an O_2 molecule and a single Ce^{4+} ion are calculated using NWChem with the corresponding basis set and functional. The sum of the first four ionization potentials of Ce (I_{Ce}^{-4} , 73.745 eV¹⁰¹) and sublimation enthalpy of Ce ($\Delta H_{\text{sub}}(\text{Ce})$, 4.380 eV¹⁰¹) are then used to obtain the reference energy of $\text{Ce}(\text{s})$.

In both M-L and QM/MM calculations, formation energies (per defect) of the unbound cation–Frenkel pair, anion–Frenkel pair, Schottky trio, and interstitial disorder defects were calculated by

$$E_{\text{Cation-Frenkel}} = \frac{1}{2}(E_f[\text{V}_{\text{Ce}}^{\text{''''}}] + E_f[\text{Ce}_i^{\text{****}}]) \quad (23)$$

$$E_{\text{Anion-Frenkel}} = \frac{1}{2}(E_f[\text{V}_{\text{O}}^{\text{**}}] + E_f[\text{O}_i^{\text{'}}]) \quad (24)$$

$$E_{\text{Schottky}} = \frac{1}{3}(E_f[\text{V}_{\text{Ce}}^{\text{''''}}] + 2E_f[\text{V}_{\text{O}}^{\text{**}}]) \quad (25)$$

$$E_{\text{Interstitial disorder}} = \frac{1}{3}(E_f[\text{Ce}_i^{\text{****}}] + 2E_f[\text{O}_i^{\text{'}}]) \quad (26)$$

3. RESULTS AND DISCUSSIONS

3.1. Strategies for Developing Robust Shell-Model Potentials. In this work, we report a framework for developing a robust shell-model IP for CeO_2 assisted by QM/MM calculations, which could also be extended to other ionic solids. First, a classical shell-model IP based on Buckingham potentials was parametrized to reproduce the bulk structure and dielectric constants. As discussed in the previous section, to make the optimal choice, we systematically reviewed the performance of several candidate potential parameter sets based on different values of the ρ parameter

in modeling defects and surface properties. Next, the optimal potential, *IP10a*, was used in hybrid QM/MM embedded-cluster models to obtain accurate references of the structure and formation energies of intrinsic defects in CeO_2 , including oxygen vacancies, cerium vacancies, oxygen interstitials, cerium interstitials, hole polaron, and electron polaron. Then, these data were used in turn to optimize the $\text{Ce}^{4+}-\text{O}^{2-}$ interactions using a more complex form that combines the Buckingham, Lennard-Jones, and Morse potentials for correcting the derivatives and an offset constant for correcting the lattice energy, *IP10b*. Finally, the $\text{Ce}^{3+}-\text{O}^{2-}$ and $\text{Ce}^{4+}-\text{O}^{1-}$ potentials were fitted based on the $\text{Ce}^{4+}-\text{O}^{2-}$ potential according to QM/MM calculations of electron and hole polarons in terms of bond length and formation energy. Based on the newly developed *IP10b*, the calculated defect structures and formation energies at the MM level of theory using the M-L approach are highly consistent with QM/MM results using hybrid DFT functionals.

3.1.1. Construction of the Reference Data Set. CeO_2 is a widely studied material with well-documented experimental measurements of physical and chemical properties. However, due to the easily reducible nature, oxygen vacancies and electron polarons in CeO_2 could significantly affect the measurements, resulting in inconsistent reports of several properties. For example, a considerable concentration of Ce^{3+} (12%–45%) was detected in many experimentally synthesized polycrystalline thin-film samples, which are very difficult to eliminate even with oxygen plasma treatment at high temperatures.^{106,107} Such a high concentration of Ce^{3+} in CeO_2 could originate not only from surface defects but also from amorphous Ce_2O_3 formed at the grain boundaries of nanocrystals.¹⁰⁶ Hence, we focus on data obtained from single

crystal and stoichiometric samples if available. The experimental lattice constant a_0 of undoped CeO_2 is typically reported to be 5.411 Å at room temperature.^{108–110} Gupta and Singh reported an a_0 of 5.401 Å at 100 K, and no data are available close to 0 K. Based on several thermal expansion experiments, we obtained an estimate for a_0 of 5.395 Å when extrapolated to 0 K.^{81,111–113} This estimate also allows us to obtain an a_0 of 5.411 Å at 300 K based on the new IP using free energy calculations within the quasi-harmonic approximation ($20 \times 20 \times 20$ k -points on the 12-atom conventional cell of CeO_2), in excellent agreement with experiment.

The $\text{O}_{2p} \rightarrow \text{Ce}_{4f}$ band gap of CeO_2 is typically reported ranging from 3.0 to 3.5 eV^{3,106,114–116} and is known to decrease with the increase in the concentrations of oxygen vacancies and Ce^{3+} .^{3,106} However, Pelli Cresi et al.¹¹⁷ recently proposed a revised value of 4 eV for the optical band gap based on steady-state and ultrafast transient absorption spectra measured on stoichiometric samples. They argued that the long absorption tail from 3 to 4 eV in the Tauc plot should be identified as the Urbach tail, further confirmed by the photobleaching in the transient absorbance measurement, which corresponds to the occupied Ce $4f$ localized state due to the rapid small polaron formation. Such an Urbach tail is also seen in nanoparticle samples with a larger band gap of 4.2–4.3 eV due to the quantum confinement effect.¹¹⁸ This conclusion is also supported by previous high-resolution electron energy loss spectroscopy (EELS) measurements on stoichiometric¹¹⁹ and fully oxidized single-crystal¹²⁰ samples, which located the unoccupied Ce_{4f} state 4–4.4 eV higher than the O_{2p} state. Hence, we consider that a band gap of 4 eV measured by Pelli Cresi et al.¹¹⁷ could be the best estimate for CeO_2 and is further employed in this work. We will compare with experimental data for the elastic constants C_{11} , C_{12} , and C_{44} ;⁸² zone-center phonon frequencies $F_{1u}(\text{TO})$, F_{2g} , and $F_{1u}(\text{LO})$;⁸² static and high-frequency dielectric constants, ϵ_0 and ϵ_∞ ;⁸³ bulk modulus B_0 ;⁸⁴ and migration barrier of oxygen vacancy $E_{V_o}^{\text{migration}}$.⁸⁵

Plane-wave DFT calculations using VASP at different levels of theory were performed alongside our semiclassical GULP simulations. The calculated lattice constants, band gaps, Born effective charges, and surface energies of CeO_2 are listed in Table 1, where we find that the hybrid functionals in our assessment set show a superior agreement with experiment. Previous work also showed that in general hybrid functionals perform much better than GGAs in describing the formation enthalpy, heat of reduction, and defect formation energy of CeO_2 .^{7,30,36} Because the PBE0 functional is implemented in both the plane-wave DFT code (VASP) and atomic-centered basis set code (NWChem), employed in our hybrid QM/MM calculations, we consistently use PBE0 results as the primary reference in the IP development. The Born effective charges and surface energies from VASP calculations, as well as the in-lattice ionic polarizabilities, defect structures, and energies from QM/MM results, were used in refining the IP. Our new IP can easily be reparameterized to reproduce the predictions from any other functional based on the same protocol.

3.1.2. Strategies for Improving the Accuracy of Shell-Model Potentials. A shell-model potential can be divided into two parts: the shell model (Y and k_2) and other parameters including short-range repulsion and dispersion interactions. The shell-model defines the ionic polarizabilities that significantly affect the dielectric properties of materials,

which play a key role in defect formation. Previous parametrizations of interatomic potentials for ceria have in common a somewhat unsatisfactory approach to choosing how the lattice polarizability is distributed between individual ions, which may not correctly reflect the physical nature of the target material. Polarizabilities have often been determined by fitting spring constants and shell charges to experimental data without consideration of the relative polarizabilities of cations and anions; it is possible to obtain a number of candidate potential sets with different shell-model parameters but with similar performances in modeling the bulk properties. An alternative to purely empirical fitting was developed by Lewis and Catlow⁷⁴ considering in-lattice polarizabilities based on gas-phase Pauling's polarizabilities of cations, which are known to be less affected by the crystal environment. By contrast, the anion polarizability varies strongly with the oxide structure and chemical composition.⁷⁴ The in-crystal ionic polarizabilities can be calculated from hybrid QM/MM embedded-cluster models (*cf.* ref 127). Here, we have employed ChemShell with NWChem as a QM driver to construct suitable embedded-cluster models and calculated the in-lattice ionic polarizability. The detailed methodology is presented in Section S1.5 of the Supporting Information.

In Table 2, we collected the calculated in-lattice polarizabilities of Ce^{4+} and O^{2-} ions using the Def2-TZVP⁹³ basis

Table 2. Calculated Intrinsic In-Lattice Ionic Polarizabilities (Bohr³) of CeO_2 Using the ChemShell Embedded-Cluster Model Compared with Their Counterparts Calculated in the Gas Phase Where Possible (O^{2-} Ions Are Unstable in the Gas Phase)

	B97-2	PBE0	BB1K	HF	CCSD	CCSD(T)
α_i (O^{2-} in CeO_2)	5.601	5.601	5.535	5.400	5.380	5.373
α_i (Ce^{4+} in CeO_2)	5.901	5.935	5.894	5.915	5.886	5.900
α_i (gas-phase Ce^{4+})	5.842	5.871	5.832	5.852	5.825	5.836

set. It can be seen that the gas-phase cation polarizability is very close to the frozen in-crystal polarizability, as has been pointed out by Lewis and Catlow.⁷⁴ The gas-phase calculations for O^{2-} are extremely basis-set-dependent, (as expected, since the O^{2-} ion is an unbound species in the gas phase), and increases from 6.293 Bohr³ using the Def2-TZVP basis set to 50.871 Bohr³ using Def2-QZVPPD¹²⁸ at the PBE0 level of theory. In the limit of a complete basis set, the ground-state solution would include an electron dissociated from the oxide ion to infinity and, therefore, an infinite polarizability. The hybrid DFT predictions are in good agreement with higher-level coupled-cluster results. The intrinsic polarizability of an ion, α_i , in the CeO_2 crystal environment does not include effects of charge transfer from or to surrounding ions, which plays a significant role in real materials, and the total polarizability of an ion is

$$\alpha = \alpha_i + \alpha_{ct} \quad (27)$$

where α_{ct} is the respective contribution from charge transfer. When fitting IP parameters, we kept the ratio of Ce^{4+} and O^{2-} polarizabilities ($\alpha = Y^2/k_2$) constant according to the QM/MM calculated polarizability data, based on a conjecture that α_{ct} is proportional to α_i . Under this methodology, a unique set of shell-model parameters can be determined that models more

Table 3. Optimized Potential *IP10b* (Defined in Equation 5) for CeO₂ Combined with Parameters for Modeling Hole (O¹⁻) and Electron (Ce³⁺) Polarons^a

(a) Short-Range Potential										
Interaction	A (eV)	ρ (Å)	C_6 (eV Å ⁶)	E (eV Å ¹²)	D (eV)	a (Å ⁻¹)	r_0 (Å)	c_0 (eV)	r_{\min} (Å)	r_{\max} (Å)
O ²⁻ –Ce ⁴⁺	1138.963021	0.417578	25.082349	1.0	-1.15172262	0.4	4.53327	-1.077767	0	5.278
O ²⁻ –Ce ³⁺	1025.066719	0.417578	25.082349	1.0	-1.036550358	0.4	4.53327	-0.9249903	0	5.532
O ¹⁻ –Ce ⁴⁺	706.157073	0.417578	25.082349	1.0	-0.714068	0.4	4.53327	-0.7462155	0	5.278
O ²⁻ –O ²⁻	22764.3	0.149	20.983768	1.0					0	15.0
O ¹⁻ –O ²⁻	22764.3	0.149	20.983768	1.0					0	15.0
O ¹⁻ –O ¹⁻	22764.3	0.149	20.983768	1.0					0	15.0
Ce ⁴⁺ –Ce ⁴⁺	1.0	0.1	30.481293	1.0					0	15.0
Ce ³⁺ –Ce ⁴⁺	1.0	0.1	30.481293	1.0					0	15.0
Ce ³⁺ –Ce ³⁺	1.0	0.1	30.481293	1.0					0	15.0

(b) Shell Model		
Species	Y (e)	k_2 (eV Å ⁻²)
Ce ⁴⁺ shell	13.85	1071.1845
Ce ³⁺ shell	12.85	1071.1845
O ²⁻ shell	-2.936345	53.022513
O ¹⁻ shell	-1.936345	53.022513

^aShort-range potentials were designed only for shell–shell interactions. A GULP-readable format is also provided in Section S3 of the Supporting Information.

accurately the relative ionic polarizabilities in solids. Our results show that Ce⁴⁺ and O²⁻ have similar polarizabilities in CeO₂. By calculating the ionic polarizabilities through eq 3, we found that most previous IPs cannot reproduce this feature.

Polarizability also determines the dispersion (London) interaction, the strength of which is usually described by the C_6 coefficient in the Buckingham interatomic potential. The similarly polarizable Ce⁴⁺ and O²⁻ in CeO₂ suggest that the C_6 coefficients for Ce⁴⁺–O²⁻, Ce⁴⁺–Ce⁴⁺, and O²⁻–O²⁻ should all be considered, whereas most of the previous IPs did not introduce the C_6 coefficients for all these interactions. We have calculated C_6 according to the Slater–Kirkwood formula¹²⁹ using the participation numbers reported by Pyper et al.¹³⁰ and our calculated polarizability data. $C_6(XY)$ is given as

$$C_6(XY) = \frac{3}{2} \frac{\alpha_X \alpha_Y}{\left(\frac{\alpha_X}{P_X}\right)^{1/2} + \left(\frac{\alpha_Y}{P_Y}\right)^{1/2}} \quad (28)$$

where P_X is the participation number of ion X (4.455 for O²⁻ and 7.901 for Ce⁴⁺ from Pyper et al.¹³⁰).

In ionic solids, the long-range electrostatic interaction contributes greatly (over 90%) to the total lattice energy. Although the short-range repulsive interaction originating from the overlapping electron densities contributes much less, the pairwise parameters in an IP largely control the bond lengths and structures and, hence, energies and physical properties. Among all the short-range interactions, the cation–anion interaction has the greatest effects due to its directly bonded nature. The cation–cation and anion–anion interactions are much weaker because of the longer interatomic distances. We note that parameter ρ in the previous Ce⁴⁺–O²⁻ Buckingham potentials varied from 0.335 Å to 0.429 Å. A small ρ with a large A or a large ρ with a small A may show only minor differences in the calculated bulk properties. However, we found that the choice of ρ is of vital importance in predicting defect and surface properties, which are typically not included in the list of fitted observables. Hence, the “best” IP derived by the fitting procedure may not be appropriate for modeling

defects and surfaces, as can be seen in the predicted incorrect relative stabilities of surfaces and defect pairs by several IPs.

To explore the effects of ρ , we parametrized several IPs based on different fixed values of ρ within the traditional Buckingham potential framework (shown in Table S2). These potentials share the same Ce⁴⁺–Ce⁴⁺ and O²⁻–O²⁻ parameters, while other parameters are fitted to minimize the sum of squares of selected observables. We used the A and ρ parameters of the O²⁻–O²⁻ Buckingham potential from Lewis and Catlow⁷⁴ since they have remarkable transferability in many ionic oxide systems and can be combined with other potentials to study dopants and solid solutions. We also put the highest fitting weights on the lattice constant (*ca.* 5.395 Å at 0 K) and static and high-frequency dielectric constants due to their critical importance in determining the accuracy of QM/MM calculations. Therefore, all the IPs we derived give accurate reproductions of the lattice constant and dielectric constants.

Figure S1 shows how the ρ parameter affects the predicted properties of CeO₂. The dark gray horizontal lines represent the reference data from experiment or DFT calculations at the PBE0 level of theory. If we only consider the bulk properties that are normally used as fitting observables, a larger value of ρ , such as $\rho = 0.37$ Å, could be the result obtained by the least-squares procedure. However, if we further consider the defect and surface properties, those IPs with a larger value of ρ produce inaccurate results for ceria. By systematically considering bulk, defect, and surface properties (discussed in Section S1.6 of the Supporting Information), we determined the IP with $\rho = 0.349$ Å as the best Buckingham potential for CeO₂, which was further used in QM/MM defect calculations. We stress that the QM/MM calculations based on *IP10a* are reliable and consistent with those based on *IP10b* since the lattice constants, dielectric constants, and ionic polarizabilities predicted by the two potentials are identical. The full set of parameters is provided in Table S2, and the performance in reproducing the properties of ceria has also been shown in Figure 1, denoted as “*IP10a*”. Within the current model, it is still impossible to reproduce simultaneously all targeted properties because the cation–anion short-range interaction

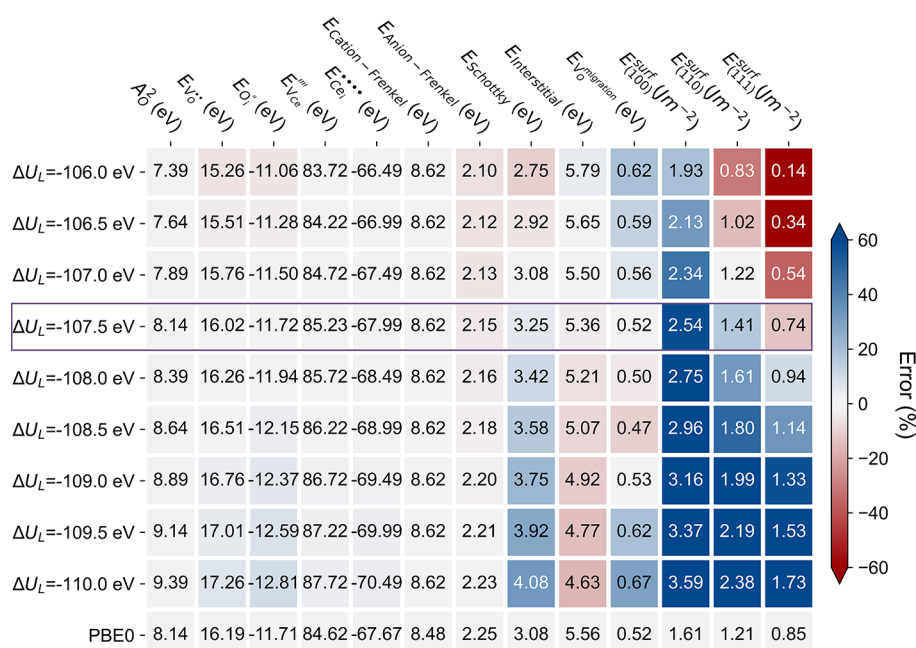


Figure 2. Effects of the predicted lattice energy ΔU_L on the calculated defect and surface properties of CeO_2 based on the new potential formula.

cannot be accurately described by a single Buckingham potential. However, we have shown here that the shell-model potential with the classical Buckingham form can qualitatively and semiquantitatively reproduce the correct atomic structure and properties of CeO_2 based on a careful selection of some critical parameters.

3.1.3. Refining the Interatomic Potential According to QM/MM Calculations. Short-range interactions in solids sometimes cannot be exactly described by a single potential adopting a simple analytical form. The Lennard-Jones potential is known to be considerably too repulsive at short bond distances.¹³¹ Although the Buckingham (and its constituent Born–Mayer) potential is a good physically justified approximation for the short-range repulsion,¹³² empirical fitting procedures could cause unwanted problems, as illustrated by the critical choice of ρ described above. Combining different forms, nevertheless, could increase the parametric space and overcome the weakness of each component to improve the accuracy.^{104,133} Derivatives of an IP determine the structure and elastic, dielectric, and phonon properties of the modeling system. The absolute potential value determines the lattice energy, which further affects the calculated energies of defects and surfaces. To obtain a robust IP, both derivatives and absolute values of the potential should be accurately determined.

We define a new analytic form for the cation–anion pairwise potential, as shown in eq 5. Parameters of the refined potential (IP10b) for CeO_2 based on this form are shown in Table 3. The sole Buckingham potential representing the short-range interaction is insufficient for a consistently accurate description of elastic, dielectric, and phonon properties. This weakness can be attributed to inaccurate potential derivatives near the first and second neighbor bond distances. Hence, a Morse-like function is superimposed on the Buckingham potential to correct these derivatives and reproduce these bulk properties accurately. The offset constant c_0 shifts down the potential curve by a constant to correct the lattice energy. Weak Lennard-Jones potentials were used to add repulsion to the

interactions at very short bond distances to overcome the Coulomb catastrophe that could occur in molecular dynamics or Monte Carlo simulations.¹³³ The overall potential is truncated at 5.278 Å where the potential energy drops to 0 eV, between the second and third Ce–O neighbor bond lengths. The resulting potential curve is shown in Figure S2, compared with previous potentials in the literature. The shell model parameters were slightly optimized for better overall performance, while the ratio of polarizabilities of Ce^{4+} and O^{2-} remained consistent with IP10a.

We here also emphasize the critical role of the lattice energy predicted by a shell-model potential in determining the accuracy of defect and surface calculations. The lattice energy ΔU_L sets an essential basis for every calculation regarding energy differences such as surface energy, defect formation energy, and migration barrier. Lattice energy is not a direct experimental observable but can be evaluated theoretically through the Born–Haber cycle based on the experimental formation enthalpy, as shown in eq 7. However, the exact value of ΔU_L requires the knowledge of the oxygen second electron affinity A_{O^2} , which is a crystal-structure-dependent variable¹³⁴ and not known from experiment. We proposed that the required ΔU_L and A_{O^2} in the IP model can be determined according to DFT-calculated surface and defect energies. As shown in Figure 2, several variants of potentials are derived based on different ΔU_L values by only varying the c_0 term while keeping all other parameters constant. As a result, these potentials share the same shape (derivatives) but differ in the absolute potential energy, thus predicting the same equilibrium-state structure but different absolute energies for defects and surfaces. The predicted defect and surface energies change considerably despite the minor differences in the predicted ΔU_L . Periodic DFT calculations of surface energies and QM/MM calculations of defect energies at the PBE0 level were employed as references to obtain the required lattice energy that gives the most accurate prediction. In IP-based surface calculations, the lattice energy mainly determines the required energy to generate the unrelaxed surfaces rather than the

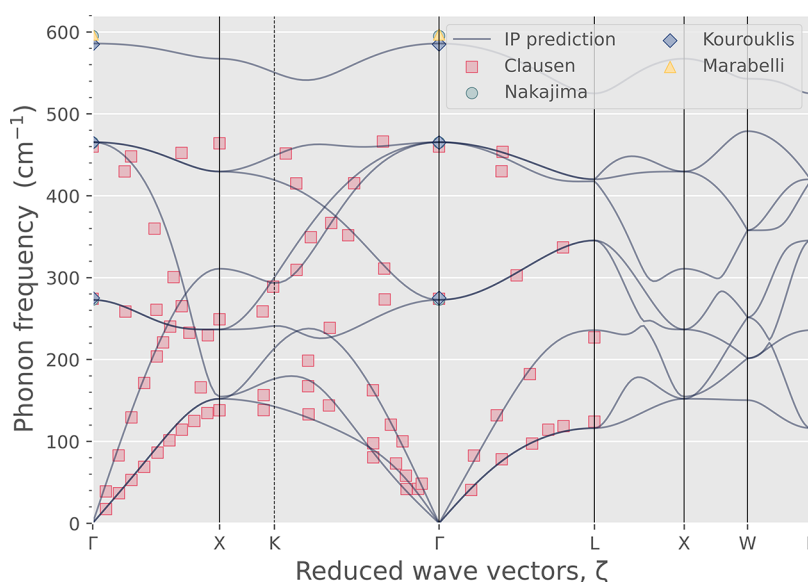


Figure 3. Calculated phonon dispersion for CeO₂ based on the new potential compared with experimental data from Clausen et al.,¹³⁶ Marabelli and Wachter,¹³⁷ Nakajima et al.,⁸² and Kourouklis et al.¹³⁸

relaxation energy. The most stable (111) surface has only 0.01 (0.05) J m⁻² relaxation energy as predicted by periodic DFT (IP-based) calculations, which could be the best reference for the target lattice energy. We found that both defect and surface calculations support that $\Delta U_L = -107.5$ eV, corresponding to an A'_O of 8.14 eV, which is employed as the final version of our CeO₂ potential (*IP10b*). We note that the new potential still has certain errors on the calculated surface energies compared with periodic DFT results. To our knowledge, the only experimental measurement of surface energies of CeO₂ was based on nanoparticle samples (which should be dominated by the most stable (111) surface) that reported an average value of 1.20 ± 0.2 J m⁻²,^{125,126} slightly higher than DFT predictions. The overestimation mainly originates from the cleavage energy before structural relaxation, which is also seen in other IP models. We have checked that the optimized surface structures are consistent with PBE0 predictions with an average error of 0.012 Å for the predicted surface and subsurface Ce–O bond lengths, suggesting a reasonably good description by the IP model.

3.1.4. Parameterization for Hole and Electron Polarons in CeO₂. Finally, we developed additional parameters for modeling localized electrons (Ce'_{Ce}) and holes (O^{\bullet}_O) in CeO₂. The electron small polaron has been experimentally observed by STM imaging and confirmed by DFT calculations on the (111) surface.^{12,30,40,43} Holes also stabilize as small polarons in CeO₂,²⁵ which is a common feature of many oxide materials.¹³⁵ The formation of electrons and holes could be modeled through the M-L approach as described by Freeman and Catlow in SnO₂.¹⁰⁰ Conventionally, electrons/holes were modeled by adding/subtracting a unit charge from the original shell charge and keeping the same core charge. However, using the same short-range potential to describe interactions between ions in different oxidation states is less accurate and usually results in several electronvolt errors in the predicted ionization potential, electron affinity, and band gap compared with experiment or DFT.^{100,104} Instead, we propose a correction scheme based on the new O²⁻–Ce⁴⁺ potentials but where we target the bond lengths and formation energies of small polarons obtained from our QM/MM calculations.

In both M-L and QM/MM calculations, vertical processes were modeled through electronic (shell) relaxation, while adiabatic processes required explicit structural optimization of the active regions. We performed QM/MM calculations to obtain the vertical and adiabatic ionization potentials and electron affinities. In the adiabatic processes, electrons and holes are self-trapped, forming small polarons in CeO₂. Before fitting the potentials for modeling the polarons, the shell charges were first corrected in line with the formal charges of Ce³⁺ and O¹⁻. Then, the coefficients in the Ce⁴⁺–O²⁻ potentials (*A* and *D*) are multiplied by a factor to correct the derivatives of the potential and reproduce the polaron structures. This factor was determined by targeting the average Ce³⁺–O²⁻/O¹⁻–Ce⁴⁺ first-neighbor bond length around the ionized species calculated by the M-L approach to correspond to PBE0 QM/MM results. Finally, the potential is offset by a c_0 constant to reproduce the polaron formation energy calculated by QM/MM. A similar procedure was used to parametrize the Ce⁴⁺–O¹⁻ potential for describing localized holes, while the vertical ionization potential was used as the reference for correcting c_0 , ensuring the alignment of the positions of VBM in both techniques for accurate formation energy calculations of charged defects. Full details of the additional parameters have been given in Table 3.

In summary, we have provided some new strategies to develop shell-model potentials with improved performance in modeling ionic materials in Section 3.1. Implementation of in-lattice ionic polarizabilities, lattice energy, defect energies, and surface energies in the potential fitting improves the description of various physical properties, while consideration of QM/MM results of charge carriers further makes it possible to model various charged defects at the MM level of theory. Based on this approach, the formation of native defects in different charge states can be reasonably described through the M-L approach, assuming that the charge carrier is well localized and trapped by defects, as is the case in CeO₂. Such an approximation gives reasonable accuracy with results comparable with DFT calculations using hybrid functionals, as will be shown in Section 3.2.

Table 4. Vertical and Adiabatic Ionization Potentials (I_{vertical} and $I_{\text{adiabatic}}$), Vertical and Adiabatic Electron Affinities (A_{vertical} and $A_{\text{adiabatic}}$), Self-Trapping Energies ($E_{\text{hole}}^{\text{ST}}$ and $E_{\text{electron}}^{\text{ST}}$) of a Hole or an Electron, the Average First-Neighbor Bond Length around the Hole or Electron ($r_{\text{Ce}^{4+}-\text{O}^{1-}}$ and $r_{\text{Ce}^{3+}-\text{O}^{2-}}$), and the Band Gap (E_{g}) of CeO₂ Calculated by the M-L Approach and QM/MM Calculations^a

	M-L (with modified shell charges) ^b	M-L (with modified shell charges and potentials) ^b	QM/MM B97-2 ^b	QM/MM PBE0 ^b	QM/MM BB1K ^b	Periodic HSE06 ^c	Periodic PBE+U ^c
I_{vertical} (eV)	9.64	5.10	4.92	5.10	5.38		
$I_{\text{adiabatic}}$ (eV)	7.11	3.78	4.35	4.41	3.80		
$E_{\text{hole}}^{\text{ST}}$ (eV)	-2.53	-1.32	-0.57	-0.69	-1.58		
$r_{\text{Ce}^{4+}-\text{O}^{1-}}$ (Å)	2.533	2.451	2.447	2.451	2.452		
A_{vertical} (eV)	0.18	0.28	0.70	0.51	0.11		
$A_{\text{adiabatic}}$ (eV)	1.44	1.20	1.31	1.20	1.50		
$E_{\text{electron}}^{\text{ST}}$ (eV)	-1.26	-0.92	-0.61	-0.69	-1.39	-0.30	-0.54
$r_{\text{Ce}^{3+}-\text{O}^{2-}}$ (Å)	2.474	2.444	2.448	2.442	2.435	2.42	
E_{g} (eV)	8.08	4.82	4.22	4.59	5.27		

^aIn M-L calculations, the first column shows the results using modified shell charges for Ce³⁺ and O¹⁻ but the same potential for Ce⁴⁺-O²⁻ interactions, while the second column shows the calculated results using *IP10b* presented in Table 3. ^bPresent work. ^cReference 30.

3.2. Performance of the New Potential in Modeling Defects in CeO₂.

The structure and properties of CeO₂ predicted by the revised potential have been shown in Figure 1, denoted as *IP10b*. Compared with *IP10a*, the revised version significantly improves the performance in many aspects: the predicted bulk modulus, elastic constants, and phonon frequencies are in excellent agreement with experiment, and the calculated defect energies are also more consistent with QM/MM predictions. Based on the new potential, we also calculated the phonon dispersion of CeO₂ at 0 K (Figure 3). Experimental results are presented in markers for comparison, derived from reflectivity by inelastic neutron scattering by Clausen et al.¹³⁶ and Marabelli and Wachter¹³⁷ and Raman scattering by Nakajima et al.⁸² and Kourouklis et al.¹³⁸ Our potential shows excellent agreement with the experimental measurements in terms of the phonon modes at the high symmetry points and acoustic mode dispersion, ensuring good accuracy for future study of thermodynamic properties of defective CeO₂ using free-energy calculations.

A detailed comparison of QM/MM and M-L calculations of the vertical and adiabatic formation energies of holes and electrons in CeO₂ is given in Table 4. Full computational details are given in Section S1.7 of the Supporting Information. For comparison, if we directly employ the Ce⁴⁺-O²⁻ short-range potential to model the localized electrons and holes without any correction (listed in the first column), as originally proposed by Freeman and Catlow,¹⁰⁰ the bond lengths around the polarons and the band gap of CeO₂ are significantly overestimated. Our corrected potential accurately reproduces the formation mechanisms of localized electrons and holes in CeO₂ and gives a more reasonable band gap. This strategy could be a general approach and extended to other systems with localized charge carriers. The self-trapping energy of the localized electron is predicted to be -0.92 eV, compared with -0.61, -0.69, and -1.39 eV by the QM/MM approach using B97-2, PBE0, and BB1K functionals, respectively. Previous periodic DFT calculations reported -0.30 eV and -0.54 eV by HSE06 and PBE+U.³⁰

The predicted band gaps by the embedded-cluster approaches are higher than the experimental values for two

reasons. First, despite the advantages in predicting bulk properties and formation energies of defects, most hybrid functionals significantly overestimate the band gap of CeO₂.^{36,37} CeO₂ is a strongly correlated *f* electron oxide, and the noncorrelated HF method predicts the band gap as 14.5 eV.³⁷ As a result, the hybrid functional that includes a higher percentage of HF exchange usually provides a worse description of the band gap of CeO₂. However, a certain percentage of HF exchange (usually 25%) is required to ensure the predictions of localized small polarons in CeO₂, or both electrons and holes will become more delocalized even when trapped by defects, which is however contrary to experiment.^{7,25,43} Second, the overestimation of the band gap is partly due to the poor description of delocalized states and quantum confinement effects by the hybrid QM/MM embedded-cluster approach. Hence, it can be seen that the predicted “band gap” through $I_{\text{vertical}} - A_{\text{vertical}}$ by the QM/MM method using the PBE0 functional (4.59 eV) is slightly higher than plane-wave periodic DFT calculations using VASP (4.38 eV) and the experimental measurement (4 eV). To counter these problems, we typically use the experimental band gap and calculated vertical ionization potential to determine the position of conduction band minimum (CBM) in QM/MM calculations.⁵⁶

3.2.1. Formation of Charged Defects in CeO₂. Using the new IP, we modeled the formation of intrinsic point defects and defect pairs in CeO₂ with the M-L and QM/MM approaches. The optimized structures of some typical defects in ceria obtained by the M-L approach are shown in Figure 4. The arrows indicate the directions and magnitudes (six times the actual length) of atomic displacements following the defect formation. We first consider the formation of atomic defects without trapped charge carriers. The formation of V_O^{••} results in an inward displacement of the six nearest O²⁻ ions by 0.275 Å, compared with 0.223–0.245 Å in the QM/MM calculations. We note that the long-range polarization effect of V_O^{••} is quite large, which causes the fourth, fifth, and sixth neighboring O²⁻ ions to move inward by 0.06 Å, 0.04 Å, and 0.02 Å, respectively. Unless a supercell with hundreds of atoms is used, periodic DFT calculations may have difficulties

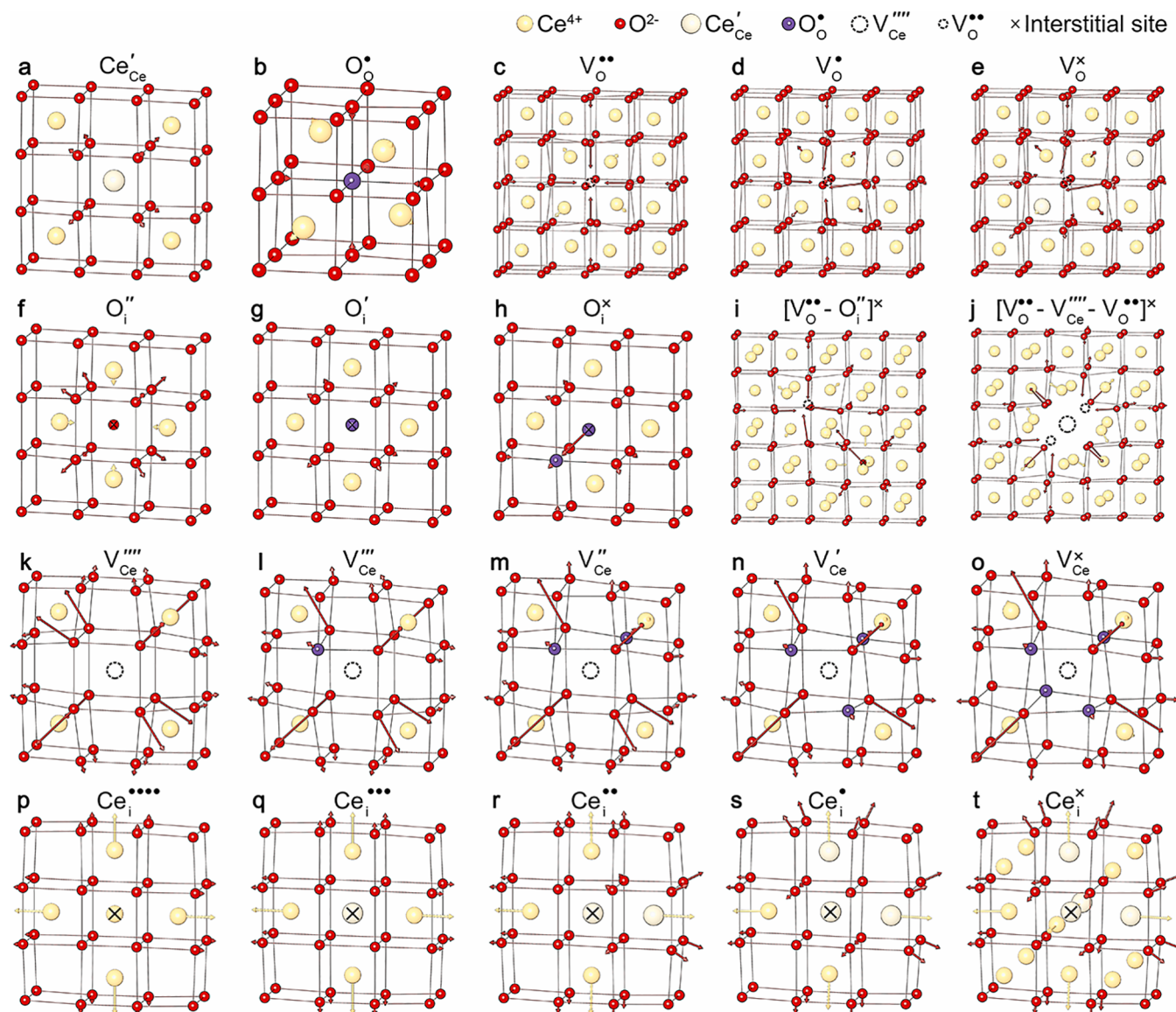


Figure 4. Defect-induced structural relaxation in CeO_2 predicted by the Mott–Littleton approach. (a) Electron polaron Ce'_{Ce} . (b) Hole polaron $\text{O}^{\bullet}_{\text{O}}$. (c–e) Oxygen vacancies V^q_{O} , $q = +2, +1, 0$. (f–h) Oxygen interstitials O^q_{i} , $q = -2, -1, 0$. (i) Bound anion–Frenkel pair $[\text{V}^{\bullet}_{\text{O}}-\text{O}^{\bullet}_{\text{i}}]^{\times}$. (j) Bound Schottky trio $[\text{V}^{\bullet}_{\text{O}}-\text{V}^{\bullet\bullet\bullet}_{\text{Ce}}-\text{V}^{\bullet}_{\text{O}}]^{\times}$. (k–o) Cerium vacancies V^q_{Ce} , $q = -4, -3, -2, -1, 0$. (p–t) Cerium interstitials Ce^q_{i} , $q = +4, +3, +2, +1, 0$. Arrows indicate directions and magnitudes of atomic displacements (magnified 6-fold to improve the clarity of images) upon relaxation.

modeling such a long-range perturbation effect. Our embedded-cluster models explicitly considered this effect because sufficiently large active regions are used. The four neighboring Ce^{4+} ions displaced outward by 0.166 Å (corresponding to 7.1% of the equilibrium bond length), which agrees well with previous DFT calculations by Sun et al. (6.8% in HSE06 and 7.1% in PBE+U).³⁰ For $\text{V}^{\bullet\bullet}_{\text{O}}$, the largest displacement was on the eight coordinating O^{2-} ions, which move away from the defect center by 0.431 Å, while the surrounding Ce^{4+} ions are barely perturbed. The $\text{O}^{\bullet}_{\text{i}}$ sits symmetrically in the center of the octahedral site. The $\text{O}^{2-}-\text{O}^{2-}$ bond length is calculated to be 2.50 Å (107.1% of the equilibrium interoxygen separation distance), which agrees well with the PBE+U prediction by Zacherle et al.²⁷ (2.52 Å and 105.9% of the PBE+U bond length). Finally, the introduction of a $\text{Ce}^{\bullet\bullet\bullet\bullet}_{\text{i}}$ results in a strong repulsion to the nearest Ce^{4+} ions, forcing them to move away by 0.357 Å (0.32–0.324 Å by previous DFT+U predictions^{25,28} and

0.337–0.349 Å by our QM/MM calculations). $\text{Ce}^{\bullet\bullet\bullet\bullet}_{\text{i}}$ has much less influence on the O^{2-} ions (displaced only by 0.096 Å). Among these types of defects, O^{2-} ions are more easily affected by defect formation than Ce^{4+} ions (except $\text{Ce}^{\bullet\bullet\bullet\bullet}_{\text{i}}$, which is less common in CeO_2 due to the relatively high formation energy). A detailed comparison of the structural relaxation due to defect formation is made in Table S3. Overall, M-L calculations show excellent agreement with previous periodic DFT and our QM/MM predictions of the defect structures.

We also studied the formation energies of different charge states of native defects using the new IP and the embedded-cluster approaches. We started from the various possible configurations of polarons trapped by oxygen vacancies in bulk ceria. Previous DFT calculations have predicted that the oxygen vacancy becomes less stable when the two polarons locate beyond the second-neighbor sites.^{29,42} This conclusion is confirmed by our M-L calculations. The calculated formation

energies of $[\text{V}_{\text{O}}^{\bullet\bullet}-\text{Ce}'_{\text{Ce}}]^{\bullet}$ in O-rich conditions when the Fermi level is at VBM are 0.049 eV, 0.046 eV, 0.306 eV, 0.267 eV, and 0.303 eV for the localized electrons at the first-, second-, third-, fourth-, and fifth-nearest neighbor sites, respectively. Hence, we only focus on the possible configurations within the second neighbor radius. For the charge-neutral oxygen vacancy $[\text{V}_{\text{O}}^{\bullet\bullet}-2\text{Ce}'_{\text{Ce}}]^{\times}$ formed in bulk ceria, the excess electrons will localize on two Ce sites (Ce'_{Ce}). As shown in Figure 5 and Table 5, there are one NN-NN, three NN-NNN, and five NNN-NNN symmetrically unique configurations on which the two Ce'_{Ce} polarons can locate.⁴¹

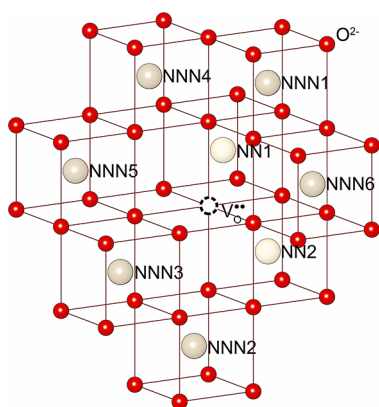


Figure 5. Electron polaron configurations in the charge-neutral oxygen vacancy $[\text{V}_{\text{O}}^{\bullet\bullet}-2\text{Ce}'_{\text{Ce}}]^{\times}$ in CeO_2 .

The calculated formation energies of all nine configurations of $[\text{V}_{\text{O}}^{\bullet\bullet}-2\text{Ce}'_{\text{Ce}}]^{\times}$ in O-rich conditions are summarized in Table 5. In general, our simulations confirm that the excess electrons have lower energies when localized on the NNN site, consistent with other DFT predictions.^{29,41,139} The most stable configuration is the NN1-NNN2 with a formation energy of 3.564 eV, and the second stable NNN1-NNN4 configuration is only 0.014 eV higher in the formation energy. Our QM/MM calculations also favor the stabilization of the NN1-NNN2 configuration against the NNN1-NNN4 configuration, consistent with the M-L predictions. The tiny energetic deviations

(<0.12 eV) among the formation energies of all the nine configurations suggest very close stabilities of different configurations, consistent with the previous periodic DFT+U study by Murgida et al.²⁹ Because the adiabatic hopping barrier for Ce'_{Ce} in CeO_2 is very low (0.15–0.2 eV^{12,140,141}), the positions of polarons could change rapidly at elevated temperatures. Previous DFT calculations predict lower formation energy at the PBE+U level (2.2–2.95 eV)^{26,29–31} and slightly higher formation energy using HSE06 (3.63–4.09 eV^{7,30,31}). Brugnoli et al.³⁸ reported 3.84 eV for the formation energy of the NN1-NN2 configuration based on the periodic model using PBE0, compared with 4.04 eV from our QM/MM model using the same functional. Burow et al.¹⁴² conducted the periodic electrostatic embedded-cluster method (PEECM) using PBE0 but obtained a much lower formation energy (3.0 eV) than our QM/MM predictions and periodic calculations from Brugnoli et al.³⁸ Our predictions at the PBE0 level of theory are also in line with the experimental heat of reduction of ceria, which is ca. 4.0 eV.^{18,19}

The same approach was used to investigate other charged defects with localized electrons and holes. Table 6 summarizes the calculated formation energies of all charge states of point defects studied by the M-L and QM/MM methods using our new IP. Figure 6 shows a direct comparison of the calculated formation energies under different conditions using the M-L approach and QM/MM calculations. These two embedded-cluster approaches present a high level of consistency in predicting the formation energies, confirming the success of our newly proposed fitting strategy for localized charge carriers. For the charge-neutral point defects compensated by electrons and holes, our predictions are in good agreement with periodic calculations. For highly charged defects, the long-range polarization effects should greatly contribute to the calculated formation energies as evaluated using the Jost correction in eq 9, which is –0.46 eV, –1.84 eV, –4.14 eV, and –7.37 eV for the ± 1 , ± 2 , ± 3 , and ± 4 charge states, respectively. These effects were typically not explicitly considered in previous supercell models. Recently, there has been increasing awareness of the application of long-range electrostatic corrections toward more quantitative predictions

Table 5. Calculated Formation Energies (eV) in O-Rich Conditions of Charge-Neutral Oxygen Vacancies Associated with Electron Polarons in Differing Configurations

Configuration	$d_{\text{Ce}^{3+}-\text{Ce}^{3+}}$	M-L ^a	QM/MM PBE0 ^d	QM/MM BB1K ^a	Periodic PBE+U ^b	Periodic PBE+U ^c	Periodic HSE06 ^c	Periodic PBE+U ^d	Periodic PBE+U ^e	Periodic HSE06 ^e	Periodic PBE0 ^f
NN1-NN2	1N	3.657	4.04		2.91	2.50	3.73	2.22	2.70	4.09	3.84
NN1-NNN6	2N	3.681			2.95						
NN1-NNN1	1N	3.673			2.93						
NN1-NNN2	3N	3.564	3.70	2.92	2.85						
NNN1-NNN2	5N	3.596			2.92						
NNN1-NNN3	4N	3.604			2.85						
NNN1-NNN4	1N	3.578	3.77	3.02	2.85	2.43	3.63				
NNN1-NNN5	3N	3.579			2.86						
NNN1-NNN6	1N	3.604			2.92						

^aPresent work. ^bPlane-wave PBE+U ($U_{\text{Ce } 4f} = 4.5$ eV) calculations using the 96-atom supercell.²⁹ ^cPlane-wave PBE+U ($U_{\text{Ce } 4f} = 5.0$ eV) and HSE06 (25% HF) calculations using the 192-atom supercell.³¹ ^dPlane-wave PBE+U ($U_{\text{Ce } 4f} = 5.0$ eV and $U_{\text{O } 2p} = 5.5$ eV) calculations using the 96-atom supercell.¹⁴³ ^ePlane-wave PBE+U ($U_{\text{Ce } 4f} = 5.0$ eV) and HSE06 (25% HF) calculations using the 96-atom supercell.³⁰ ^fPlane-wave PBE0 (25% HF) calculations using the 96-atom supercell.³⁸

Table 6. Calculated Formation Energies (eV) of Intrinsic Point Defects in CeO₂ in O-Rich Conditions^a

Defect reactions	M-L ^b	QM/MM B97-2 ^b	QM/MM PBE0 ^b	QM/MM BB1K ^b	Periodic HSE06 ^c	Periodic PBE+U ^c	Periodic PBE+U ^d	Periodic PBE+U ^e
(a) Oxygen vacancy								
$\text{O}_\text{O}^\times \rightarrow \text{V}_\text{O}^{\bullet\bullet} + \frac{1}{2}\text{O}_2(\text{g}) + 2e'$	4.57	4.59	4.61	3.45	5.0	4.3	4.7	4.43
$\text{O}_\text{O}^\times \rightarrow \text{V}_\text{O}^\bullet + \frac{1}{2}\text{O}_2(\text{g}) + e'$	4.05	3.52	3.84	2.89	4.5	3.4	4.13	3.66
$\text{O}_\text{O}^\times \rightarrow \text{V}_\text{O}^\times + \frac{1}{2}\text{O}_2(\text{g})$	3.56	3.11	3.70	2.92	4.09	2.7	3.16	2.8
(b) Oxygen interstitial								
$\frac{1}{2}\text{O}_2(\text{g}) \rightarrow \text{O}_\text{i}' + 2h^\bullet$	7.72	7.86	7.87	8.08			7.40	4.41
$\frac{1}{2}\text{O}_2(\text{g}) \rightarrow \text{O}_\text{i}' + h^\bullet$	4.04	5.28	5.14	4.81			4.49	3.60
$\frac{1}{2}\text{O}_2(\text{g}) \rightarrow \text{O}_\text{i}^\times$	2.54	3.39	3.17	2.51			1.82	2.79
(c) Cerium vacancy								
$\text{Ce}_{\text{Ce}}^\times + \frac{1}{2}\text{O}_2(\text{g}) \rightarrow \text{V}_{\text{Ce}}^{\bullet\bullet\bullet\bullet} + \text{CeO}_2(\text{s}) + 4h^\bullet$	16.60	14.87	16.01	17.44			9.0	7.39
$\text{Ce}_{\text{Ce}}^\times + \frac{1}{2}\text{O}_2(\text{g}) \rightarrow \text{V}_{\text{Ce}}^{\bullet\bullet\bullet} + \text{CeO}_2(\text{s}) + 3h^\bullet$	14.05	12.46	13.43	14.35			8.0	6.32
$\text{Ce}_{\text{Ce}}^\times + \frac{1}{2}\text{O}_2(\text{g}) \rightarrow \text{V}_{\text{Ce}}^{\bullet\bullet} + \text{CeO}_2(\text{s}) + 2h^\bullet$	11.58	11.00	11.81	12.24			7.1	6.52
$\text{Ce}_{\text{Ce}}^\times + \frac{1}{2}\text{O}_2(\text{g}) \rightarrow \text{V}_{\text{Ce}}^\bullet + \text{CeO}_2(\text{s}) + h^\bullet$	9.20	8.71	9.31	9.20			5.8	6.81
$\text{Ce}_{\text{Ce}}^\times + \frac{1}{2}\text{O}_2(\text{g}) \rightarrow \text{V}_{\text{Ce}}^\times + \text{CeO}_2(\text{s})$	6.91	7.35	7.77	7.14			5.0	7.39
(d) Cerium interstitial								
$\text{CeO}_2(\text{s}) \rightarrow \text{Ce}_\text{i}^{\bullet\bullet\bullet\bullet} + \frac{1}{2}\text{O}_2(\text{g}) + 4e'$	16.63	17.60	16.94	15.48			13.45	14.46
$\text{CeO}_2(\text{s}) \rightarrow \text{Ce}_\text{i}^{\bullet\bullet\bullet} + \frac{1}{2}\text{O}_2(\text{g}) + 3e'$	14.68	15.86	15.41	14.02			12.95	13.55
$\text{CeO}_2(\text{s}) \rightarrow \text{Ce}_\text{i}^{\bullet\bullet} + \frac{1}{2}\text{O}_2(\text{g}) + 2e'$	13.8	14.62	14.43	13.17			12.75	12.57
$\text{CeO}_2(\text{s}) \rightarrow \text{Ce}_\text{i}^\bullet + \frac{1}{2}\text{O}_2(\text{g}) + e'$	13.05	13.44	13.71	12.61			12.05	11.69
$\text{CeO}_2(\text{s}) \rightarrow \text{Ce}_\text{i}^\times + \frac{1}{2}\text{O}_2(\text{g})$	12.44	12.64	13.00	12.19			11.69	10.9

^aReaction energies are reported assuming holes formed at the VBM and electrons at the CBM (using the calculated VBM at each level of theory and experimental 4 eV band gap for obtaining CBM). ^bPresent work. ^cPlane-wave PBE+U ($U_{\text{Ce } 4f} = 5.0$ eV) and HSE06 (25% HF) calculations using the 96-atom supercell. ^dPlane-wave PBE+U ($U_{\text{Ce } 4f} = 4.0$ eV and $U_{\text{O } 2p} = 4.0$ eV) calculations using the 96-atom supercell with a nonlinear core-corrected (NLCC) norm-conserving pseudopotential for Ce. ^ePlane-wave PBE+U ($U_{\text{Ce } 4f} = 5.0$ eV) calculations using the 96-atom supercell with PAW.²⁷

of defect formation energies using supercell approaches.⁵⁰ Apart from the long-range effect, it should also be noted that there are significant differences between the PBE+U and HSE06 predictions on $\text{V}_\text{O}^{\bullet\bullet}$ and V_O^\times using the standard PAW method based on the same setting.³⁰ Therefore, for these defects in higher charge states such as $\text{V}_{\text{Ce}}^{\bullet\bullet\bullet\bullet}$ and $\text{Ce}_\text{i}^{\bullet\bullet\bullet\bullet}$, it is not surprising that PBE+U calculations might have several electron volts difference compared with hybrid functional predictions, although there is no corresponding reference data available.

Our M-L predictions of the formation energies of charge-neutral defect pairs and trios are also in good agreement with QM/MM predictions. When an anion–Frenkel pair is formed, a lattice oxygen ion occupies an octahedral interstitial site, leaving an oxygen vacancy. The formation energy is predicted to be 2.15 eV per defect (4.30 eV for the total defect reaction) by our potential model at infinite separation (2.23 eV, 2.24 eV,

and 1.77 eV at the QM/MM B97-2, PBE0, and BB1K levels of theory, respectively, 2.07–2.08 eV by periodic PBE+U calculations,^{27,28} and 1.83 eV by experiment¹⁴⁴). In our M-L calculations, we observed the recombination behavior of bound anion–Frenkel pairs in the nearest (2.34 Å) and next-nearest (4.47 Å) separations. The first stable anion–Frenkel pair has a separation distance of 5.88 Å with a total formation energy of 3.85 eV (viewed as a defect cluster), yielding a binding energy of 0.45 eV. The second stable pair has a slightly higher formation energy of 3.98 eV due to the larger separation (7.01 Å). Our M-L calculations predict a similar critical stabilization distance of the bound anion–Frenkel pair as reported by Huang et al.²⁸ using periodic PBE+U calculations (5.95 Å). The M-L calculated formation energy of the unbound Schottky trio [$\text{V}_{\text{Ce}}^{\bullet\bullet\bullet\bullet}$] + 2[$\text{V}_\text{O}^{\bullet\bullet}$] is of 3.25 eV per defect, compared with 2.69 eV by B97-2, 3.08 eV by PBE0, and

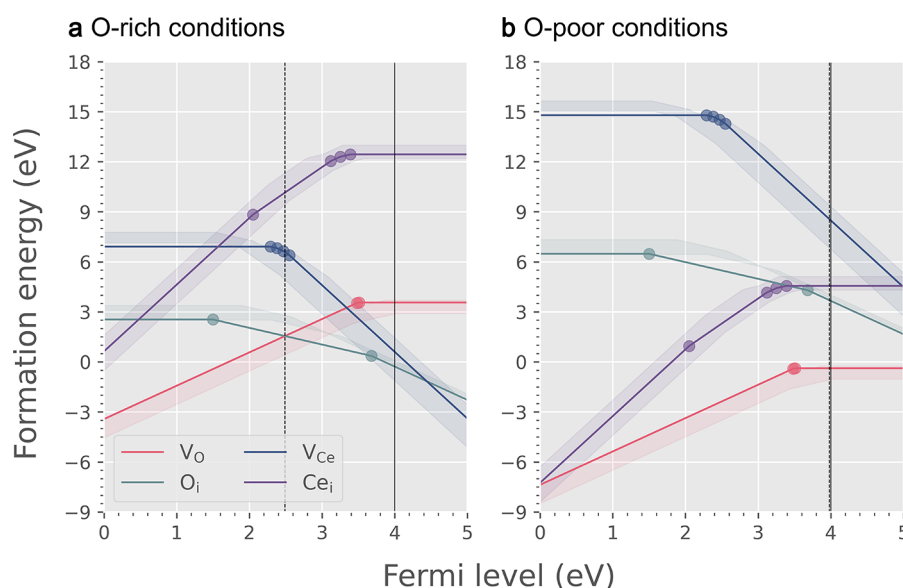


Figure 6. Calculated formation energies of intrinsic defects in CeO₂ under different growth conditions using the M-L approach. Only the most stable charge states for each type of defect are shown. Solid circles indicate the thermodynamic transition levels. The lighter regions were determined by the minimum and maximum values obtained from B97-2, PBE0, and BB1K QM/MM calculations. The vertical solid lines show the position of the CBM according to the experimental band gap of 4 eV. The vertical dashed lines indicate the calculated self-consistent Fermi energy in each growth condition at 100 K, i.e., the low-temperature regime. (a) In O-rich/Ce-poor conditions. (b) In O-poor/Ce-rich conditions.

2.78 eV by BB1K functionals in QM/MM. Previous periodic PBE+U studies reported 2.29 eV by Zacherle et al.²⁷ According to our M-L calculations, Schottky trios can form stable bound complexes with formation energies of 5.18 eV, 5.22 eV, and 5.86 eV for two oxygen vacancies aligned along the $\langle 111 \rangle$, $\langle 110 \rangle$, and $\langle 100 \rangle$ directions, respectively, with respect to the cation vacancy. The corresponding binding energies are quite high due to the high charges and close proximity of the cation and anion vacancies, whose distances are 4.58 Å, 4.53 Å, and 3.89 Å, respectively. Our predicted formation energy for the bound Schottky trio is slightly higher than other PBE+U calculations of 3.66 eV by Keating et al.²⁵ and 3.86 eV by Huang et al.²⁸ The calculated formation energy for the interstitial disorder ($[\text{Ce}_i^{\bullet\bullet\bullet}] + 2[\text{O}_i^{\prime\prime}]$) is 5.36 eV by the M-L approach, also in good agreement with the predictions of 5.77 eV, 5.56 eV, and 5.21 eV at the QM/MM B97-2, PBE0, and BB1K levels of theory. We also predicted a higher formation energy for the cation–Frenkel pair ($[\text{V}_{\text{Ce}}^{\prime\prime\prime}] + [\text{Ce}_i^{\bullet\bullet\bullet}]$) than other periodic PBE+U calculations (8.62 eV compared with 5.8–6.3 eV^{26–28}). However, the M-L prediction agrees well with our QM/MM results (8.24 eV, 8.48 eV, and 8.46 eV at the B97-2, PBE0, and BB1K levels of theory, respectively).

The anion–Frenkel pair ($[\text{V}_{\text{O}}^{\bullet\bullet}] + [\text{O}_i^{\prime\prime}]$) is predicted to be the dominant defect pair in bulk ceria, consistent with a recent neutron scattering study.¹⁶ This behavior is similar to other cubic fluorite crystals such as UO₂ and cubic ZrO₂.^{72,145} Oxygen vacancy formation is of crucial importance in bulk ceria, which can repeatedly absorb and release oxygen in catalytic reactions through the Mars–van Krevelen mechanism.^{9,10} Furthermore, the $\text{V}_{\text{O}}^{\bullet\bullet}$ migration barrier is very low (0.53 eV predicted by our potential, 0.5–0.6 eV by previous DFT and experimental studies^{30,85,146–148}), which could be further reduced by the surrounding $\text{Ce}_{\text{Ce}}^{\prime}$ polarons on the surfaces,^{12,140} ensuring good ionic conductivity in SOFC applications. All these features make this material versatile in energy and catalytic applications.

The energetic difference in predictions between the embedded-cluster approaches and periodic PBE+U results could mainly originate from the differences in DFT functional and long-range polarization effects. As illustrated before, the periodic PBE+U approach may not be accurate enough for the formation energy of highly charged defects, while our QM/MM calculations that employ hybrid functionals and consider long-range polarization should be more reliable and target the defect formation at the dilute limit. Overall, *IP10b* accurately describes defect structures and formation mechanisms in ceria, which could be useful for investigating more complex defect clusters and partially reduced phases that are computationally too expensive for first-principles calculations. Moreover, our potential model for modeling holes and electron polarons is highly transferable. Using the same correction approach, one can reproduce the predictions of other hybrid functionals.

3.2.2. Thermodynamic Defect Processes in Bulk CeO₂. The formation energy of a point defect depends on the position of the Fermi level (electronic chemical potential) and chemical potentials of exchanged species according to eq 8, which will be further affected by conditions, especially oxygen partial pressure P and temperature.¹⁰⁷ As summarized by Reuter and Scheffler,¹⁴⁹ the relationship between the oxygen chemical potential $\mu_{\text{O}}(T, P)$ and oxygen partial pressure P can be obtained by

$$\mu_{\text{O}}(T, P) = \mu_{\text{O}}(T, P^0) + \frac{1}{2}kT \ln \frac{P}{P^0} \quad (29)$$

$$\begin{aligned} \mu_{\text{O}}(T, P^0) = & \frac{1}{2}[H(T, P^0, \text{O}_2) - H(0 \text{ K}, P^0, \text{O}_2)] \\ & - \frac{1}{2}T[S(T, P^0, \text{O}_2) - S(0 \text{ K}, P^0, \text{O}_2)] \end{aligned} \quad (30)$$

where $P^0 = 1 \text{ atm}$ is typically defined as the zero state, $\mu_{\text{O}}(0 \text{ K}, P^0) = \frac{1}{2}E_{\text{O}_2} = 0 \text{ eV}$, H is the enthalpy, and S is

entropy. Using the experimental enthalpy and entropy data,¹⁵⁰ we calculated the value of μ_{O} at various reaction conditions. As shown in Figure 7a, μ_{O} decreases with increase in temperature

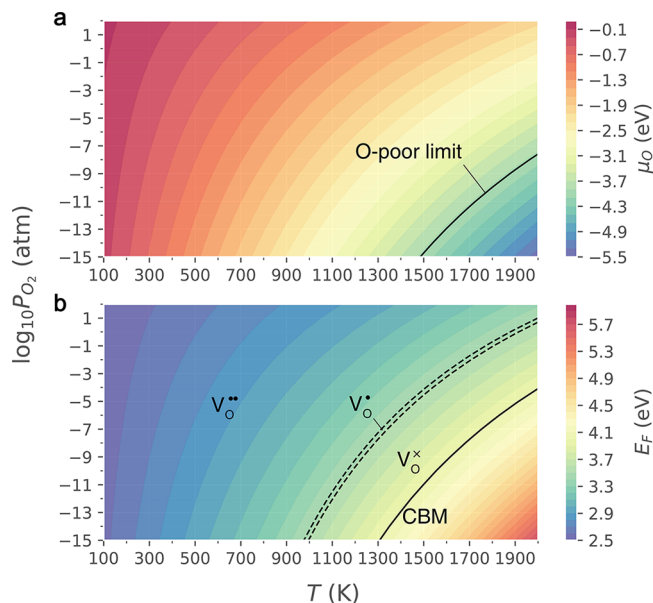


Figure 7. Variations of the (a) oxygen chemical potential and (b) calculated self-consistent Fermi level relative to VBM with temperature and oxygen partial pressure.

or decrease in P . In the case of CeO_2 , an extreme reducing condition (e.g., $P = 2.3 \times 10^{-10}$ atm at 1800 K) is required to reach the O-poor limit of $\mu_{\text{O min}} = -3.94$ eV at which Ce_2O_3 becomes more stable than CeO_2 . In realistic systems, the formation energies of defects always lie between the two limits shown in Figure 6.

The Fermi level of CeO_2 is in turn also affected by temperature and oxygen partial pressure.¹⁰⁷ Variation of the Fermi level influences further the dominant defect type, energetics of charge states, and concentrations of defects in solids. The self-consistent Fermi energy (shown in Figure 7b) was determined using the SC-FERMI code¹⁵¹ based on the M-L defect formation energies and density of states of the pristine CeO_2 (obtained using VASP with PBE0 functional, where the unoccupied states were shifted downward to reproduce the experimental band gap of 4 eV). In the O-rich limit, the Fermi level lies *ca.* 2.5 eV above the VBM and favors the formation of doubly ionized $\text{V}_{\text{O}}^{\bullet\bullet}$. These vacancies could be compensated by acceptor defects such as O_i'' and O_i' or electrons that are not trapped at the vacancy sites. With the increase in temperature or decrease in oxygen partial pressure, the Fermi level rises toward the CBM, which could further support the stabilization of $\text{V}_{\text{O}}^{\bullet}$ and $\text{V}_{\text{O}}^{\times}$ with trapped electron polarons. An electrical conductivity study by Tuller and Nowick⁴⁴ on single-crystal CeO_{2-x} samples also concluded that $\text{V}_{\text{O}}^{\bullet\bullet}$ is dominant at small x in CeO_{2-x} ($x < 10^{-3}$), with a transition to singly ionized $\text{V}_{\text{O}}^{\bullet}$ at greater x under reduced P , confirming our predictions. The thermodynamic transition level $\varepsilon(q_1/q_2)$ is defined as the energy of an adiabatic ionization process changing the charge state q_1 of the defect to another charge state q_2 . It can be obtained as the electron Fermi level where the formation energies of two charge states of a point defect are equal or using the following formula:³⁹

$$\varepsilon(q_1/q_2) = \frac{E_f(X^{q_1}, E_F = 0) - E_f(X^{q_2}, E_F = 0)}{q_2 - q_1} \quad (31)$$

where $E_f(X^q, E_F = 0)$ is the formation energy of the defect X with the charge state q when the Fermi level is at the valence band maximum (VBM, $E_F = 0$). The thermodynamic transition level indicates the relative stability of the two charge states. When $E_F < \varepsilon(q_1/q_2)$, the charge state q_1 is stable and *vice versa*. The calculated thermodynamic transition levels of oxygen vacancy are shown as dashed lines in Figure 7b. In our M-L calculations, $\varepsilon(+2/+1) = 3.48$ eV and $\varepsilon(+1/0) = 3.51$ eV above the VBM. Sun et al.³⁰ have compared DFT PBE+U and HSE06 predictions using the supercell approach with an appropriate correction scheme on charged defects. They also obtained high transition levels for oxygen vacancies using the HSE06 functional ($\varepsilon(+2/+1) = 3.1$ eV and $\varepsilon(+1/0) = 3.2$ eV), but their PBE+U calculations yielded much lower values of $\varepsilon(+2/+1) = 1.45$ eV and $\varepsilon(+1/0) = 1.65$ eV. This difference could originate from the accuracy of the predicted band gap from the DFT functionals.

Our previous discussion focused on the equilibrium-state defect formation in bulk CeO_2 at the dilute limit, without considering the extrinsic doping and surface effects. Even trace dopants, or impurities can considerably affect the position of the Fermi level and defect formation.^{26,70,152} Further, we should note that the formation energies of $\text{V}_{\text{O}}^{\times}$ on or near the surfaces are much lower than their counterparts in bulk, which could be rationalized by a decrease in the coordination of atoms exposed at the topmost surface layer. Previous PBE+U calculations reported an energetically favorable formation of $\text{V}_{\text{O}}^{\times}$ in the subsurface layer of $\text{CeO}_2(111)$ with a formation energy of *ca.* 1.8 eV compared with 2.85 eV in bulk.^{24,153} The formation energies of $\text{V}_{\text{O}}^{\times}$ on less stable $\text{CeO}_2(110)$ and $\text{CeO}_2(100)$ surfaces are predicted to be even lower by Ganduglia-Pirovano et al.²⁴ and are 1.06 and 1.35 eV, respectively. Such low formation energies of $\text{V}_{\text{O}}^{\times}$ should result in nonnegligible shifts of transition levels toward the VBM and would favor the trapping of excess electrons near the surfaces, as experimentally captured by STM images.^{40,43} This observation is, in fact, quite general. For example, recently, Wang and Yin¹⁵⁴ also found that iodine vacancies in $\text{CH}_3\text{NH}_3\text{PbI}_3$ formed in the bulk and on the surface have significant differences in the transition level and effects on photovoltaic performance. Returning to CeO_2 , reduction in practice always starts from the near-surface layers, resulting in the localization and segregation of excess electrons, which could lead to further reconstruction into alternative ordered phases such as $\text{CeO}_{1.68}$, Ce_7O_{12} , $\text{Ce}_{11}\text{O}_{20}$, and Ce_3O_5 .^{16,110,155,156} Trace dopants or unintended impurities including divalent¹⁵⁷ and trivalent¹⁵⁸ metal ions and surface adsorbates such as fluorine¹⁵⁹ and hydroxyls¹⁶⁰ could also become the charge-compensating species for $\text{V}_{\text{O}}^{\bullet\bullet}$ and have a large impact on the Fermi level and defect concentrations. Our calculations show that, with the increase in temperature or decrease in oxygen partial pressure, the Fermi level rises in bulk CeO_2 , and singly ionized $\text{V}_{\text{O}}^{\bullet}$ and charge-neutral $\text{V}_{\text{O}}^{\times}$ become dominant before the formation of ordered reduced phases. A complete understanding of the partial reduction behavior of ceria requires further investigation using, e.g., free energy calculations, Monte Carlo, or molecular dynamics techniques^{161–164} to consider explicitly entropic effects of defect formation and defect–defect interactions, which will be investigated in future research based on our new potential.

4. CONCLUSIONS

We have proposed a new strategy for deriving shell-model interatomic potentials based on hybrid QM/MM embedded-cluster calculations of ionic polarizabilities, defect structures, and formation energies. A new potential has been developed for CeO₂, with a distinctive performance in predicting the structure, elastic, dielectric, defect, surface, phonon, and thermodynamic properties compared with experimental measurements and *ab initio* calculations. In particular, the calculated structures and formation energies of polarons, various charged states of native defects, and defect pairs in CeO₂ achieved a high level of consistency between the M-L calculations and QM/MM results. Benefiting from our new potential, one could provide more insights into the complex defect chemistry of CeO₂. These developments will enable future work on defect formation at elevated temperatures using free energy calculations; partial reduction and nonstoichiometry based on molecular dynamics and Monte Carlo simulations; and the role of surface defects in catalytic reactions using QM/MM techniques. This novel strategy for developing robust shell-model potentials capable of predicting accurate defect properties could be further extended to other ionic systems.

■ ASSOCIATED CONTENT

SI Supporting Information

The Supporting Information is available free of charge at <https://pubs.acs.org/doi/10.1021/acs.chemmater.2c03019>.

Additional information on the methodological details of plane-wave DFT calculations, interatomic-potential-based calculations, QM/MM interface treatment, Mott–Littleton and QM/MM calculations on several properties of ceria; supplementary data on variants of Buckingham potentials with different ρ values and their performances, shell-model potential parameters in the literature, comparison of atomic displacements due to defect formation, and the new potential *IP10b* in GULP-readable format (PDF)

■ AUTHOR INFORMATION

Corresponding Authors

C. Richard A. Catlow – *Kathleen Lonsdale Materials Chemistry, Department of Chemistry, University College London, London WC1H 0AJ, United Kingdom; School of Chemistry, Cardiff University, Cardiff CF10 1AT, United Kingdom; orcid.org/0000-0002-1341-1541; Email: c.r.a.catlow@ucl.ac.uk*

Alexey A. Sokol – *Kathleen Lonsdale Materials Chemistry, Department of Chemistry, University College London, London WC1H 0AJ, United Kingdom; orcid.org/0000-0003-0178-1147; Email: a.sokol@ucl.ac.uk*

Authors

Xingfan Zhang – *Kathleen Lonsdale Materials Chemistry, Department of Chemistry, University College London, London WC1H 0AJ, United Kingdom; orcid.org/0000-0003-0852-4194*

Lei Zhu – *Kathleen Lonsdale Materials Chemistry, Department of Chemistry, University College London, London WC1H 0AJ, United Kingdom*

Qing Hou – *Kathleen Lonsdale Materials Chemistry, Department of Chemistry, University College London,*

London WC1H 0AJ, United Kingdom; Institute of Photonic Chips, University of Shanghai for Science and Technology, Shanghai 200093, China

Jingcheng Guan – *Kathleen Lonsdale Materials Chemistry, Department of Chemistry, University College London, London WC1H 0AJ, United Kingdom*

You Lu – *Scientific Computing Department, STFC Daresbury Laboratory, Warrington, Cheshire WA4 4AD, United Kingdom; orcid.org/0000-0002-7524-4179*

Thomas W. Keal – *Scientific Computing Department, STFC Daresbury Laboratory, Warrington, Cheshire WA4 4AD, United Kingdom; orcid.org/0000-0001-8747-3975*

John Buckeridge – *School of Engineering, London South Bank University, London SE1 0AA, United Kingdom*

Complete contact information is available at:

<https://pubs.acs.org/10.1021/acs.chemmater.2c03019>

Notes

The authors declare no competing financial interest.

■ ACKNOWLEDGMENTS

The authors acknowledge the use of the THOMAS, YOUNG, and ARCHER2 U.K. National Supercomputing Service (<http://www.archer2.ac.uk>) via membership of U.K.'s HEC Materials Chemistry Consortium, which is funded by EPSRC (Grant Nos. EP/P020194, EP/T022213, and EP/R029431). We also acknowledge funding provided by EPSRC under Grant Nos. EP/W014580, EP/R001847, EP/K038419, and EP/I030662. Q.H. acknowledges funding from the Shanghai Pujiang Program (Grant 22PJ1411300). X.Z. acknowledges the support from the China Scholarship Council (CSC) and Han Yu for useful discussions.

■ REFERENCES

- Montini, T.; Melchionna, M.; Monai, M.; Fornasiero, P. Fundamentals and catalytic applications of CeO₂-based materials. *Chem. Rev.* **2016**, *116* (10), 5987–6041.
- Schmitt, R.; Nanning, A.; Kraynis, O.; Korobko, R.; Frenkel, A. I.; Lubomirsky, I.; Haile, S. M.; Rupp, J. L. A review of defect structure and chemistry in ceria and its solid solutions. *Chem. Soc. Rev.* **2020**, *49* (2), 554–592.
- Xu, Y.; Mofarah, S. S.; Mehmood, R.; Cazorla, C.; Koshy, P.; Sorrell, C. C. Design strategies for ceria nanomaterials: untangling key mechanistic concepts. *Mater. Horiz.* **2021**, *8* (1), 102–123.
- Chueh, W. C.; Falter, C.; Abbott, M.; Scipio, D.; Furler, P.; Haile, S. M.; Steinfeld, A. High-flux solar-driven thermochemical dissociation of CO₂ and H₂O using nonstoichiometric ceria. *Science* **2010**, *330* (6012), 1797–1801.
- Chang, K.; Zhang, H.; Cheng, M.-j.; Lu, Q. Application of Ceria in CO₂ Conversion Catalysis. *ACS Catal.* **2020**, *10* (1), 613–631.
- Liu, Z.; Huang, E.; Orozco, I.; Liao, W.; Palomino, R. M.; Rui, N.; Duchoň, T.; Nemsák, S.; Grinter, D. C.; Mahapatra, M.; et al. Water-promoted interfacial pathways in methane oxidation to methanol on a CeO₂-Cu₂O catalyst. *Science* **2020**, *368* (6490), 513–517.
- Paier, J.; Penschke, C.; Sauer, J. Oxygen defects and surface chemistry of ceria: quantum chemical studies compared to experiment. *Chem. Rev.* **2013**, *113* (6), 3949–3985.
- Maurer, F.; Jelic, J.; Wang, J.; Gänzler, A.; Dolcet, P.; Wöll, C.; Wang, Y.; Studt, F.; Casapu, M.; Grunwaldt, J.-D. Tracking the formation, fate and consequence for catalytic activity of Pt single sites on CeO₂. *Nature Catal.* **2020**, *3* (10), 824–833.
- Muravev, V.; Spezzati, G.; Su, Y.-Q.; Parastaev, A.; Chiang, F.-K.; Longo, A.; Escudero, C.; Kosinov, N.; Hensen, E. J. Interface

dynamics of Pd-CeO₂ single-atom catalysts during CO oxidation. *Nature Catal.* **2021**, *4* (6), 469–478.

(10) Xing, F.; Nakaya, Y.; Yasumura, S.; Shimizu, K.-i.; Furukawa, S. Ternary platinum-cobalt-indium nanoalloy on ceria as a highly efficient catalyst for the oxidative dehydrogenation of propane using CO₂. *Nature Catal.* **2022**, *5* (1), 55–65.

(11) Andersson, D. A.; Simak, S. I.; Skorodumova, N. V.; Abrikosov, I. A.; Johansson, B. Optimization of ionic conductivity in doped ceria. *Proc. Natl. Acad. Sci. U. S. A.* **2006**, *103* (10), 3518–3521.

(12) Zhang, D.; Han, Z.-K.; Murgida, G. E.; Ganduglia-Pirovano, M. V.; Gao, Y. Oxygen-vacancy dynamics and entanglement with polaron hopping at the reduced CeO₂(111) surface. *Phys. Rev. Lett.* **2019**, *122* (9), 096101.

(13) Cheisson, T.; Schelter, E. J. Rare earth elements: Mendeleev's bane, modern marvels. *Science* **2019**, *363* (6426), 489–493.

(14) Skorodumova, N.; Simak, S.; Lundqvist, B. I.; Abrikosov, I.; Johansson, B. Quantum origin of the oxygen storage capability of ceria. *Phys. Rev. Lett.* **2002**, *89* (16), 166601.

(15) Franchini, C.; Reticcioli, M.; Setvin, M.; Diebold, U. Polarons in materials. *Nat. Rev. Mater.* **2021**, *6* (7), 560–586.

(16) Luo, S.; Li, M.; Fung, V.; Sumpter, B. G.; Liu, J.; Wu, Z.; Page, K. New Insights into the Bulk and Surface Defect Structures of Ceria Nanocrystals from Neutron Scattering Study. *Chem. Mater.* **2021**, *33* (11), 3959–3970.

(17) Kröger, F.; Vink, H. Relations between the concentrations of imperfections in crystalline solids. In *Solid state physics*; Elsevier: 1956; Vol. 3, pp 307–435.

(18) Zinkevich, M.; Djurovic, D.; Aldinger, F. Thermodynamic modelling of the cerium-oxygen system. *Solid State Ionics* **2006**, *177* (11–12), 989–1001.

(19) Trovarelli, A.; Fornasiero, P. *Catalysis by ceria and related materials*; World Scientific: 2013; Vol. 12, DOI: 10.1142/p870.

(20) Nolan, M.; Parker, S. C.; Watson, G. W. The electronic structure of oxygen vacancy defects at the low index surfaces of ceria. *Surf. Sci.* **2005**, *595* (1–3), 223–232.

(21) Migani, A.; Vayssilov, G. N.; Bromley, S. T.; Illas, F.; Neyman, K. M. Dramatic reduction of the oxygen vacancy formation energy in ceria particles: a possible key to their remarkable reactivity at the nanoscale. *J. Mater. Chem.* **2010**, *20* (46), 10535–10546.

(22) Murgida, G. E.; Ganduglia-Pirovano, M. V. Evidence for subsurface ordering of oxygen vacancies on the reduced CeO₂(111) surface using density-functional and statistical calculations. *Phys. Rev. Lett.* **2013**, *110* (24), 246101.

(23) Trovarelli, A.; Llorca, J. Ceria catalysts at nanoscale: how do crystal shapes shape catalysis? *ACS Catal.* **2017**, *7* (7), 4716–4735.

(24) Pérez-Bailac, P.; Lustemberg, P. G.; Ganduglia-Pirovano, M. V. Facet-dependent stability of near-surface oxygen vacancies and excess charge localization at CeO₂ surfaces. *J. Phys.: Condens. Matter* **2021**, *33* (50), 504003.

(25) Keating, P. R.; Scanlon, D. O.; Morgan, B. J.; Galea, N. M.; Watson, G. W. Analysis of intrinsic defects in CeO₂ using a Koopmans-like GGA+ U approach. *J. Phys. Chem. C* **2012**, *116* (3), 2443–2452.

(26) Keating, P. R.; Scanlon, D. O.; Watson, G. W. Computational testing of trivalent dopants in CeO₂ for improved high-κ dielectric behaviour. *J. Mater. Chem. C* **2013**, *1* (6), 1093–1098.

(27) Zacherle, T.; Schriever, A.; De Souza, R.; Martin, M. Ab initio analysis of the defect structure of ceria. *Phys. Rev. B* **2013**, *87* (13), 134104.

(28) Huang, B.; Gillen, R.; Robertson, J. Study of CeO₂ and its native defects by density functional theory with repulsive potential. *J. Phys. Chem. C* **2014**, *118* (42), 24248–24256.

(29) Murgida, G. E.; Ferrari, V.; Ganduglia-Pirovano, M. V.; Llois, A. M. Ordering of oxygen vacancies and excess charge localization in bulk ceria: a DFT+ U study. *Phys. Rev. B* **2014**, *90* (11), 115120.

(30) Sun, L.; Huang, X.; Wang, L.; Janotti, A. Disentangling the role of small polarons and oxygen vacancies in CeO₂. *Phys. Rev. B* **2017**, *95* (24), 245101.

(31) Du, D.; Wolf, M. J.; Hermansson, K.; Broqvist, P. Screened hybrid functionals applied to ceria: Effect of Fock exchange. *Phys. Rev. B* **2018**, *97* (23), 235203.

(32) Plata, J. J.; Márquez, A. M.; Sanz, J. F. Communication: Improving the density functional theory+U description of CeO₂ by including the contribution of the O 2p electrons. *J. Chem. Phys.* **2012**, *136* (4), 041101.

(33) Schäfer, T.; Daelman, N.; López, N. Cerium oxides without U: The role of many-electron correlation. *J. Phys. Chem. Lett.* **2021**, *12* (27), 6277–6283.

(34) Branda, M. M.; Castellani, N. J.; Grau-Crespo, R.; de Leeuw, N. H.; Hernandez, N. C.; Sanz, J. F.; Neyman, K. M.; Illas, F. On the difficulties of present theoretical models to predict the oxidation state of atomic Au adsorbed on regular sites of CeO₂(111). *J. Chem. Phys.* **2009**, *131* (9), 094702.

(35) Da Silva, J. L.; Ganduglia-Pirovano, M. V.; Sauer, J.; Bayer, V.; Kresse, G. Hybrid functionals applied to rare-earth oxides: The example of ceria. *Phys. Rev. B* **2007**, *75* (4), 045121.

(36) Graciani, J.; Márquez, A. M.; Plata, J. J.; Ortega, Y.; Hernández, N. C.; Meyer, A.; Zicovich-Wilson, C. M.; Sanz, J. F. Comparative study on the performance of hybrid DFT functionals in highly correlated oxides: the case of CeO₂ and Ce₂O₃. *J. Chem. Theory Comput.* **2011**, *7* (1), 56–65.

(37) Brugnoli, L.; Ferrari, A. M.; Civalleri, B.; Pedone, A.; Menziani, M. C. Assessment of density functional approximations for highly correlated oxides: the case of CeO₂ and Ce₂O₃. *J. Chem. Theory Comput.* **2018**, *14* (9), 4914–4927.

(38) Brugnoli, L.; Menziani, M. C.; Urata, S.; Pedone, A. Development and application of a ReaxFF reactive force field for cerium oxide/water interfaces. *J. Phys. Chem. A* **2021**, *125* (25), 5693–5708.

(39) Freysoldt, C.; Grabowski, B.; Hickel, T.; Neugebauer, J.; Kresse, G.; Janotti, A.; Van de Walle, C. G. First-principles calculations for point defects in solids. *Rev. Mod. Phys.* **2014**, *86* (1), 253.

(40) Esch, F.; Fabris, S.; Zhou, L.; Montini, T.; Africh, C.; Fornasiero, P.; Comelli, G.; Rosei, R. Electron localization determines defect formation on ceria substrates. *Science* **2005**, *309* (5735), 752–755.

(41) Wang, B.; Xi, X.; Cormack, A. N. Chemical strain and point defect configurations in reduced ceria. *Chem. Mater.* **2014**, *26* (12), 3687–3692.

(42) Minervini, L.; Zacate, M. O.; Grimes, R. W. Defect cluster formation in M₂O₃-doped CeO₂. *Solid State Ionics* **1999**, *116* (3–4), 339–349.

(43) Jerratsch, J.-F.; Shao, X.; Nilius, N.; Freund, H.-J.; Popa, C.; Ganduglia-Pirovano, M. V.; Burow, A. M.; Sauer, J. Electron localization in defective ceria films: A study with scanning-tunneling microscopy and density-functional theory. *Phys. Rev. Lett.* **2011**, *106* (24), 246801.

(44) Tuller, H.; Nowick, A. Defect structure and electrical properties of nonstoichiometric CeO₂ single crystals. *J. Electrochem. Soc.* **1979**, *126* (2), 209.

(45) Thajudheen, T.; Dixon, A. G.; Gardonio, S.; Arçon, I.; Valant, M. Oxygen vacancy-related cathodoluminescence quenching and polarons in CeO₂. *J. Phys. Chem. C* **2020**, *124* (37), 19929–19936.

(46) Serra, J.; Borrás-Morell, J.; García-Baños, B.; Balaguer, M.; Plaza-González, P.; Santos-Blasco, J.; Catalán-Martínez, D.; Navarrete, L.; Catalá-Civera, J. M. Hydrogen production via microwave-induced water splitting at low temperature. *Nat. Energy* **2020**, *5* (11), 910–919.

(47) Zhang, Q.; Bu, J.; Wang, J.; Sun, C.; Zhao, D.; Sheng, G.; Xie, X.; Sun, M.; Yu, L. Highly efficient hydrogenation of nitrobenzene to aniline over Pt/CeO₂ catalysts: The shape effect of the support and key role of additional Ce³⁺ sites. *ACS Catal.* **2020**, *10* (18), 10350–10363.

(48) Kantorovich, L. N. Elimination of the long-range dipole interaction in calculations with periodic boundary conditions. *Phys. Rev. B* **1999**, *60* (23), 15476–15479.

- (49) Lany, S.; Zunger, A. Assessment of correction methods for the band-gap problem and for finite-size effects in supercell defect calculations: Case studies for ZnO and GaAs. *Phys. Rev. B* **2008**, *78* (23), 235104.
- (50) Walsh, A. Correcting the corrections for charged defects in crystals. *npj Comput. Mater.* **2021**, *7* (1), 72.
- (51) Sokol, A. A.; French, S. A.; Bromley, S. T.; Catlow, C. R. A.; van Dam, H. J.; Sherwood, P. Point defects in ZnO. *Faraday Discuss.* **2007**, *134*, 267–282.
- (52) Walsh, A.; Buckeridge, J.; Catlow, C. R. A.; Jackson, A. J.; Keal, T. W.; Miskufova, M.; Sherwood, P.; Shevlin, S. A.; Watkins, M. B.; Woodley, S. M.; Sokol, A. A. Limits to Doping of Wide Band Gap Semiconductors. *Chem. Mater.* **2013**, *25* (15), 2924–2926.
- (53) Richter, N. A.; Sicolo, S.; Levchenko, S. V.; Sauer, J.; Scheffler, M. Concentration of vacancies at metal-oxide surfaces: Case study of MgO(100). *Phys. Rev. Lett.* **2013**, *111* (4), 045502.
- (54) Buckeridge, J.; Catlow, C. R. A.; Scanlon, D. O.; Keal, T. W.; Sherwood, P.; Miskufova, M.; Walsh, A.; Woodley, S. M.; Sokol, A. A. Determination of the Nitrogen Vacancy as a Shallow Compensating Center in GaN Doped with Divalent Metals. *Phys. Rev. Lett.* **2015**, *114* (1), 016405.
- (55) Catlow, C. R. A.; Buckeridge, J.; Farrow, M. R.; Logsdail, A. J.; Sokol, A. A. Quantum Mechanical/Molecular Mechanical (QM/MM) Approaches. *Handbook of Solid State Chemistry* **2017**, 647–680.
- (56) Buckeridge, J.; Catlow, C. R. A.; Farrow, M.; Logsdail, A. J.; Scanlon, D.; Keal, T.; Sherwood, P.; Woodley, S.; Sokol, A.; Walsh, A. Deep vs shallow nature of oxygen vacancies and consequent n-type carrier concentrations in transparent conducting oxides. *Phys. Rev. Mater.* **2018**, *2* (5), 054604.
- (57) Mott, N.; Littleton, M. Conduction in polar crystals. I. Electrolytic conduction in solid salts. *Trans. Faraday Soc.* **1938**, *34*, 485–499.
- (58) Catlow, C. R. A. Mott-Littleton calculations in solid-state chemistry and physics. *J. Chem. Soc., Faraday Trans. 2* **1989**, *85* (5), 335–340.
- (59) Lidiard, A. B. The Mott-Littleton method: an introductory survey. *J. Chem. Soc., Faraday Trans. 2* **1989**, *85* (5), 341–349.
- (60) Sherwood, P.; de Vries, A. H.; Guest, M. F.; Schreckenbach, G.; Catlow, C. R. A.; French, S. A.; Sokol, A. A.; Bromley, S. T.; Thiel, W.; Turner, A. J.; et al. QUASI: A general purpose implementation of the QM/MM approach and its application to problems in catalysis. *J. Mol. Struct.: THEOCHEM* **2003**, *632* (1–3), 1–28.
- (61) Sokol, A. A.; Bromley, S. T.; French, S. A.; Catlow, C. R. A.; Sherwood, P. Hybrid QM/MM embedding approach for the treatment of localized surface states in ionic materials. *Int. J. Quantum Chem.* **2004**, *99* (5), 695–712.
- (62) Dick, B. G.; Overhauser, A. W. Theory of the Dielectric Constants of Alkali Halide Crystals. *Phys. Rev.* **1958**, *112* (1), 90–103.
- (63) Xie, Z.; Sui, Y.; Buckeridge, J.; Catlow, C. R. A.; Keal, T. W.; Sherwood, P.; Walsh, A.; Farrow, M. R.; Scanlon, D. O.; Woodley, S. M.; et al. Donor and acceptor characteristics of native point defects in GaN. *J. Phys. D: Appl. Phys.* **2019**, *52* (33), 335104.
- (64) Sauer, J. Ab Initio Calculations for Molecule-Surface Interactions with Chemical Accuracy. *Acc. Chem. Res.* **2019**, *52* (12), 3502–3510.
- (65) Zhao, Q.; Zhang, X.; Martirez, J. M. P.; Carter, E. A. Benchmarking an embedded adaptive sampling configuration interaction method for surface reactions: H₂ desorption from and CH₄ dissociation on Cu(111). *J. Chem. Theory Comput.* **2020**, *16* (11), 7078–7088.
- (66) Shi, B. X.; Kapil, V.; Zen, A.; Chen, J.; Alavi, A.; Michaelides, A. General embedded cluster protocol for accurate modeling of oxygen vacancies in metal-oxides. *J. Chem. Phys.* **2022**, *156* (12), 124704.
- (67) Grimes, R. W.; Catlow, C. R. A. Modeling Localized Defects in Ionic Materials Using Mott-Littleton and Embedded Quantum Cluster Methodology. *J. Am. Ceram. Soc.* **1990**, *73* (11), 3251–3256.
- (68) Grimes, R. W.; Catlow, C. R. A.; Stoneham, A. M. Quantum-mechanical cluster calculations and the Mott-Littleton methodology. *J. Chem. Soc., Faraday Trans. 2* **1989**, *85* (5), 485–495.
- (69) Catlow, C. R. A.; French, S. A.; Sokol, A. A.; Al-Sunaidi, A. A.; Woodley, S. M. Zinc oxide: A case study in contemporary computational solid state chemistry. *J. Comput. Chem.* **2008**, *29* (13), 2234–2249.
- (70) Butler, V.; Catlow, C.; Fender, B.; Harding, J. Dopant ion radius and ionic conductivity in cerium dioxide. *Solid State Ionics* **1983**, *8* (2), 109–113.
- (71) Sayle, T. X. T.; Parker, S. C.; Catlow, C. R. A. The role of oxygen vacancies on ceria surfaces in the oxidation of carbon monoxide. *Surf. Sci.* **1994**, *316* (3), 329–336.
- (72) Grimes, R.; Catlow, C. R. A. The stability of fission products in uranium dioxide. *Philos. Trans. R. Soc., A* **1991**, *335* (1639), 609–634.
- (73) Vyas, S.; Grimes, R. W.; Gay, D. H.; Rohl, A. L. Structure, stability and morphology of stoichiometric ceria crystallites. *J. Chem. Soc., Faraday Trans.* **1998**, *94* (3), 427–434.
- (74) Lewis, G.; Catlow, C. Potential models for ionic oxides. *J. Phys. C: Solid State Phys.* **1985**, *18* (6), 1149.
- (75) Gotte, A.; Spångberg, D.; Hermansson, K.; Baudin, M. Molecular dynamics study of oxygen self-diffusion in reduced CeO₂. *Solid State Ionics* **2007**, *178* (25–26), 1421–1427.
- (76) Walsh, A.; Woodley, S. M.; Catlow, C. R. A.; Sokol, A. A. Potential energy landscapes for anion Frenkel-pair formation in ceria and india. *Solid State Ionics* **2011**, *184* (1), 52–56.
- (77) Gerhardt-Anderson, R.; Zamani-Noor, F.; Nowick, A.; Catlow, C.; Cormack, A. Study of Sc₂O₃-doped ceria by anelastic relaxation. *Solid State Ionics* **1983**, *9*, 931–936.
- (78) Cormack, A.; Catlow, C.; Nowick, A. Theoretical studies of off-centre Sc³⁺ impurities in CeO₂. *J. Phys. Chem. Solids* **1989**, *50* (2), 177–181.
- (79) Sayle, T. X.; Parker, S. C.; Catlow, C. R. A. Surface oxygen vacancy formation on CeO₂ and its role in the oxidation of carbon monoxide. *J. Chem. Soc., Chem. Commun.* **1992**, No. 14, 977–978.
- (80) Sayle, T. X. T.; Caddeo, F.; Zhang, X.; Sakhivel, T.; Das, S.; Seal, S.; Ptasinska, S.; Sayle, D. C. Structure-Activity Map of Ceria Nanoparticles, Nanocubes, and Mesoporous Architectures. *Chem. Mater.* **2016**, *28* (20), 7287–7295.
- (81) Secura, S.; Campbell, W. J. *Thermal expansion and phase inversion of rare-earth oxides*; U.S. Department of the Interior, Bureau of Mines: 1961; Vol. 5847.
- (82) Nakajima, A.; Yoshihara, A.; Ishigame, M. Defect-induced Raman spectra in doped CeO₂. *Phys. Rev. B* **1994**, *50* (18), 13297.
- (83) Mochizuki, S. Infrared optical properties of cerium dioxide. *Phys. Status Solidi B* **1982**, *114* (1), 189–199.
- (84) Gerward, L.; Olsen, J. S.; Petit, L.; Vaitheeswaran, G.; Kanchana, V.; Svane, A. Bulk modulus of CeO₂ and PrO₂—An experimental and theoretical study. *J. Alloys Compd.* **2005**, *400* (1–2), 56–61.
- (85) Steele, B. C. H.; Floyd, J. M. Oxygen Self-Diffusion and Electrical Transport Properties of Nonstoichiometric Ceria and Ceria Solid Solutions. *Proc. Brit. Ceramic Soc.* **1971**, 55–76.
- (86) Kresse, G.; Furthmüller, J. Efficient iterative schemes for ab initio total-energy calculations using a plane-wave basis set. *Phys. Rev. B* **1996**, *54* (16), 11169.
- (87) Born, M.; Huang, K. *Dynamical Theory of Crystal Lattices*; Clarendon Press: 1954.
- (88) Gale, J. D.; Rohl, A. L. The general utility lattice program (GULP). *Mol. Simul.* **2003**, *29* (5), 291–341.
- (89) Gale, J. D. GULP: A computer program for the symmetry-adapted simulation of solids. *J. Chem. Soc., Faraday Trans.* **1997**, *93* (4), 629–637.
- (90) Norgett, M. A. *General formulation of the problem of calculating the energies of lattice defects in ionic crystals*; Atomic Energy Research Establishment: 1974; Harwell Technical Report R.7650 HL74/335.
- (91) Lu, Y.; Farrow, M. R.; Fayon, P.; Logsdail, A. J.; Sokol, A. A.; Catlow, C. R. A.; Sherwood, P.; Keal, T. W. Open-source, python-based redevelopment of the chemshell multiscale QM/MM environment. *J. Chem. Theory Comput.* **2019**, *15* (2), 1317–1328.
- (92) Valiev, M.; Bylaska, E. J.; Govind, N.; Kowalski, K.; Straatsma, T. P.; Van Dam, H. J.; Wang, D.; Nieplocha, J.; Apra, E.; Windus, T.

- L.; et al. NWChem: A comprehensive and scalable open-source solution for large scale molecular simulations. *Comput. Phys. Commun.* **2010**, *181* (9), 1477–1489.
- (93) Weigend, F.; Ahlrichs, R. Balanced basis sets of split valence, triple zeta valence and quadruple zeta valence quality for H to Rn: Design and assessment of accuracy. *Phys. Chem. Chem. Phys.* **2005**, *7* (18), 3297–3305.
- (94) Desmarais, J. K.; Erba, A.; Dovesi, R. Generalization of the periodic LCAO approach in the CRYSTAL code to g-type orbitals. *Theor. Chem. Acc.* **2018**, *137* (2), 28.
- (95) El-Kelany, K. E.; Ravoux, C.; Desmarais, J.; Cortona, P.; Pan, Y.; Tse, J.; Erba, A. Spin localization, magnetic ordering, and electronic properties of strongly correlated Ln_2O_3 sesquioxides (Ln = La, Ce, Pr, Nd). *Phys. Rev. B* **2018**, *97* (24), 245118.
- (96) Dolg, M.; Stoll, H.; Preuss, H. Energy-adjusted ab initio pseudopotentials for the rare earth elements. *J. Chem. Phys.* **1989**, *90* (3), 1730–1734.
- (97) Wilson, P. J.; Bradley, T. J.; Tozer, D. J. Hybrid exchange-correlation functional determined from thermochemical data and ab initio potentials. *J. Chem. Phys.* **2001**, *115* (20), 9233–9242.
- (98) Adamo, C.; Barone, V. Toward reliable density functional methods without adjustable parameters: The PBE0 model. *J. Chem. Phys.* **1999**, *110* (13), 6158–6170.
- (99) Zhao, Y.; Lynch, B. J.; Truhlar, D. G. Development and assessment of a new hybrid density functional model for thermochemical kinetics. *J. Phys. Chem. A* **2004**, *108* (14), 2715–2719.
- (100) Freeman, C.; Catlow, C. A computer modeling study of defect and dopant states in SnO_2 . *J. Solid State Chem.* **1990**, *85* (1), 65–75.
- (101) Haynes, W. M. *CRC handbook of chemistry and physics*; CRC Press: 2014.
- (102) Chaibi, W.; Peláez, R.; Blondel, C.; Drag, C.; Delsart, C. Effect of a magnetic field in photodetachment microscopy. *Eur. Phys. J. D* **2010**, *58* (1), 29–37.
- (103) Waddington, T. Lattice energies and their significance in inorganic chemistry. *Adv. Inorg. Chem. Radiochem.* **1959**, *1*, 157–221.
- (104) Hou, Q.; Buckeridge, J.; Lazauskas, T.; Mora-Fonz, D.; Sokol, A. A.; Woodley, S. M.; Catlow, C. R. A. Defect formation in In_2O_3 and SnO_2 : A new atomistic approach based on accurate lattice energies. *J. Mater. Chem. C* **2018**, *6* (45), 12386–12395.
- (105) Jost, W. Diffusion and electrolytic conduction in crystals (ionic semiconductors). *J. Chem. Phys.* **1933**, *1* (7), 466–475.
- (106) Patsalas, P.; Logothetidis, S.; Sygellou, L.; Kennou, S. Structure-dependent electronic properties of nanocrystalline cerium oxide films. *Phys. Rev. B* **2003**, *68* (3), 035104.
- (107) Wardenga, H. F.; Klein, A. Surface potentials of (111), (110) and (100) oriented CeO_{2-x} thin films. *Appl. Surf. Sci.* **2016**, *377*, 1–8.
- (108) McCullough, J. D. An X-ray study of the rare-earth oxide systems: $\text{Ce}^{\text{IV}}-\text{Nd}^{\text{III}}$, $\text{Cr}^{\text{IV}}-\text{Pr}^{\text{III}}$, $\text{Ce}^{\text{IV}}-\text{Pr}^{\text{IV}}$ and $\text{Pr}^{\text{IV}}-\text{Nd}^{\text{III}}$. *J. Am. Chem. Soc.* **1950**, *72* (3), 1386–1390.
- (109) Bevan, D.; Kordis, J. Mixed oxides of the type MO_2 (fluorite)— M_2O_3 —I oxygen dissociation pressures and phase relationships in the system $\text{CeO}_2-\text{Ce}_2\text{O}_3$ at high temperatures. *J. Inorg. Nucl. Chem.* **1964**, *26* (9), 1509–1523.
- (110) Kümmerle, E.; Heger, G. The structures of $\text{C-Ce}_2\text{O}_{3+\delta}$, Ce_7O_{12} , and $\text{Ce}_{11}\text{O}_{20}$. *J. Solid State Chem.* **1999**, *147* (2), 485–500.
- (111) Rossignol, S.; Gérard, F.; Mesnard, D.; Kappenstein, C.; Duprez, D. Structural changes of Ce-Pr-O oxides in hydrogen: a study by in situ X-ray diffraction and Raman spectroscopy. *J. Mater. Chem.* **2003**, *13* (12), 3017–3020.
- (112) Yashima, M.; Kobayashi, S.; Yasui, T. Crystal structure and the structural disorder of ceria from 40 to 1497 °C. *Solid State Ionics* **2006**, *177* (3–4), 211–215.
- (113) GUPTA, M. L.; Singh, S. Thermal Expansion of CeO_2 , Ho_2O_3 , and Lu_2O_3 from 100° to 300° K by an X-Ray Method. *J. Am. Ceram. Soc.* **1970**, *53* (12), 663–665.
- (114) Wuilloud, E.; Delley, B.; Schneider, W.-D.; Baer, Y. Spectroscopic Evidence for Localized and Extended f-Symmetry States in CeO_2 . *Phys. Rev. Lett.* **1984**, *53* (2), 202.
- (115) Orel, Z. C.; Orel, B. Optical properties of pure CeO_2 and mixed $\text{CeO}_2/\text{SnO}_2$ thin film coatings. *Phys. Status Solidi B* **1994**, *186* (1), K33–K36.
- (116) Guo, S.; Arwin, H.; Jacobsen, S.; Järrendahl, K.; Helmersson, U. A spectroscopic ellipsometry study of cerium dioxide thin films grown on sapphire by rf magnetron sputtering. *J. Appl. Phys.* **1995**, *77* (10), 5369–5376.
- (117) Pelli Cresi, J. S.; Di Mario, L.; Catone, D.; Martelli, F.; Paladini, A.; Turchini, S.; D'Addato, S.; Luches, P.; O'Keeffe, P. Ultrafast Formation of Small Polarons and the Optical Gap in CeO_2 . *J. Phys. Chem. Lett.* **2020**, *11* (14), 5686–5691.
- (118) Moreno, O. P.; Pérez, R. G.; Merino, R. P.; Portillo, M. C.; Tellez, G. H.; Rosas, E. R.; Tototzintle, M. Z. CeO_2 nanoparticles growth by chemical bath and its thermal annealing treatment in air atmosphere. *Optik* **2017**, *148*, 142–150.
- (119) Pfau, A.; Schierbaum, K. The electronic structure of stoichiometric and reduced CeO_2 surfaces: an XPS, UPS and HREELS study. *Surf. Sci.* **1994**, *321* (1–2), 71–80.
- (120) Mullins, D.; Overbury, S.; Huntley, D. Electron spectroscopy of single crystal and polycrystalline cerium oxide surfaces. *Surf. Sci.* **1998**, *409* (2), 307–319.
- (121) Molinari, M.; Parker, S. C.; Sayle, D. C.; Islam, M. S. Water adsorption and its effect on the stability of low index stoichiometric and reduced surfaces of ceria. *J. Phys. Chem. C* **2012**, *116* (12), 7073–7082.
- (122) Buckeridge, J.; Scanlon, D.; Walsh, A.; Catlow, C.; Sokol, A. Dynamical response and instability in ceria under lattice expansion. *Phys. Rev. B* **2013**, *87* (21), 214304.
- (123) Jiang, H. Revisiting the GW approach to d- and f-electron oxides. *Phys. Rev. B* **2018**, *97* (24), 245132.
- (124) Debnath, S.; Islam, M.; Khan, M. Optical properties of CeO_2 thin films. *Bull. Mater. Sci.* **2007**, *30* (4), 315–319.
- (125) Hayun, S.; Ushakov, S. V.; Navrotsky, A. Direct measurement of surface energy of CeO_2 by differential scanning calorimetry. *J. Am. Ceram. Soc.* **2011**, *94* (11), 3679–3682.
- (126) Hayun, S.; Shvareva, T. Y.; Navrotsky, A. Nanocerium Energetics of surfaces, interfaces and water adsorption. *J. Am. Ceram. Soc.* **2011**, *94* (11), 3992–3999.
- (127) Fowler, P. W.; Pyper, N. In-crystal ionic polarizabilities derived by combining experimental and ab initio results. *Proc. R. Soc. London, Ser. A* **1985**, *398* (1815), 377–393.
- (128) Rappoport, D.; Furche, F. Property-optimized Gaussian basis sets for molecular response calculations. *J. Chem. Phys.* **2010**, *133* (13), 134105.
- (129) Slater, J. C.; Kirkwood, J. G. The van der Waals forces in gases. *Phys. Rev.* **1931**, *37* (6), 682.
- (130) Fowler, P.; Harding, J.; Pyper, N. The polarizabilities and dispersion coefficients for ions in the solid group IV oxides. *J. Phys.: Condens. Matter* **1994**, *6* (48), 10593.
- (131) Van Vleet, M. J.; Misquitta, A. J.; Stone, A. J.; Schmidt, J. R. Beyond born-mayer: Improved models for short-range repulsion in ab initio force fields. *J. Chem. Theory Comput.* **2016**, *12* (8), 3851–3870.
- (132) Buckingham, R. A. The classical equation of state of gaseous helium, neon and argon. *Proc. R. Soc. A* **1938**, *168* (933), 264–283.
- (133) Mora-Fonz, D.; Schön, J. C.; Prehl, J.; Woodley, S. M.; Catlow, C. R. A.; Shluger, A.; Sokol, A. A. Real and Virtual Polymorphism of Titanium Selenide with Robust Interatomic Potentials. *J. Mater. Chem. A* **2020**, *8*, 14054.
- (134) Walsh, A.; Butler, K. T. Prediction of electron energies in metal oxides. *Acc. Chem. Res.* **2014**, *47* (2), 364–372.
- (135) Schirmer, O. F. O-bound small polarons in oxide materials. *J. Phys.: Condens. Matter* **2006**, *18* (43), R667.
- (136) Clausen, K.; Hayes, W.; Macdonald, J. E.; Osborn, R.; Schnabel, P. G.; Hutchings, M. T.; Magerl, A. Inelastic neutron scattering investigation of the lattice dynamics of ThO_2 and CeO_2 . *J. Chem. Soc., Faraday Trans. 2* **1987**, *83* (7), 1109–1112.
- (137) Marabelli, F.; Wachter, P. Covalent insulator CeO_2 : optical reflectivity measurements. *Phys. Rev. B* **1987**, *36* (2), 1238.

- (138) Kourouklis, G.; Jayaraman, A.; Espinosa, G. High-pressure Raman study of CeO₂ to 35 GPa and pressure-induced phase transformation from the fluorite structure. *Phys. Rev. B* **1988**, *37* (8), 4250.
- (139) Ganduglia-Pirovano, M. V.; Da Silva, J. L. F.; Sauer, J. Density-Functional Calculations of the Structure of Near-Surface Oxygen Vacancies and Electron Localization on CeO₂(111). *Phys. Rev. Lett.* **2009**, *102* (2), 026101.
- (140) Su, Y.-Q.; Filot, I. A.; Liu, J.-X.; Tranca, I.; Hensen, E. J. Charge transport over the defective CeO₂(111) surface. *Chem. Mater.* **2016**, *28* (16), 5652–5658.
- (141) Castleton, C. W.; Lee, A.; Kullgren, J. Benchmarking Density Functional Theory Functionals for Polarons in Oxides: Properties of CeO₂. *J. Phys. Chem. C* **2019**, *123* (9), 5164–5175.
- (142) Burrow, A. M.; Sierka, M.; Döbler, J.; Sauer, J. Point defects in CaF₂ and CeO₂ investigated by the periodic electrostatic embedded cluster method. *J. Chem. Phys.* **2009**, *130* (17), 174710.
- (143) Ganduglia-Pirovano, M. V.; Murgida, G. E.; Ferrari, V.; Llois, A. M. a. Comment on “Oxygen Vacancy Ordering and Electron Localization in CeO₂: Hybrid Functional Study”. *J. Phys. Chem. C* **2017**, *121* (38), 21080–21083.
- (144) Stratton, T. G.; Tuller, H. L. Thermodynamic and transport studies of mixed oxides. The CeO₂-UO₂ system. *J. Chem. Soc., Faraday Trans. 2* **1987**, *83* (7), 1143–1156.
- (145) Liu, X.-Y.; Sickafus, K. E. Lanthanum energetics in cubic ZrO₂ and UO₂ from DFT and DFT+ U studies. *J. Nucl. Mater.* **2011**, *414* (2), 217–220.
- (146) Fuda, K.; Kishio, K.; Yamauchi, S.; Fueki, K.; Onoda, Y. ¹⁷O NMR study of Y₂O₃-doped CeO₂. *J. Phys. Chem. Solids* **1984**, *45* (11–12), 1253–1257.
- (147) Nolan, M.; Fearon, J. E.; Watson, G. W. Oxygen vacancy formation and migration in ceria. *Solid State Ionics* **2006**, *177* (35–36), 3069–3074.
- (148) Wang, D.; Park, D.; Griffith, J.; Nowick, A. Oxygen-ion conductivity and defect interactions in yttria-doped ceria. *Solid State Ionics* **1981**, *2* (2), 95–105.
- (149) Reuter, K.; Scheffler, M. Composition, structure, and stability of RuO₂(110) as a function of oxygen pressure. *Phys. Rev. B* **2001**, *65* (3), 035406.
- (150) Stull, D. R. *JANAF Thermochemical Tables*; Clearinghouse: 1965; Vol. 1.
- (151) Buckeridge, J. Equilibrium point defect and charge carrier concentrations in a material determined through calculation of the self-consistent Fermi energy. *Comput. Phys. Commun.* **2019**, *244*, 329–342.
- (152) Hu, Z.; Metiu, H. Effect of dopants on the energy of oxygen-vacancy formation at the surface of ceria: Local or global? *J. Phys. Chem. C* **2011**, *115* (36), 17898–17909.
- (153) Ganduglia-Pirovano, M. V.; Da Silva, J. L.; Sauer, J. Density-functional calculations of the structure of near-surface oxygen vacancies and electron localization on CeO₂(111). *Phys. Rev. Lett.* **2009**, *102* (2), 026101.
- (154) Wang, J.; Yin, W.-J. Revisiting the Iodine Vacancy Surface Defects to Rationalize Passivation Strategies in Perovskite Solar Cells. *J. Phys. Chem. Lett.* **2022**, *13*, 6694–6700.
- (155) Murgida, G. E.; Ferrari, V.; Llois, A. M.; Ganduglia-Pirovano, M. V. Reduced CeO₂(111) ordered phases as bulk terminations: Introducing the structure of Ce₃O₅. *Phys. Rev. Mater.* **2018**, *2* (8), 083609.
- (156) Olbrich, R.; Murgida, G. E.; Ferrari, V.; Barth, C.; Llois, A. M.; Reichling, M.; Ganduglia-Pirovano, M. V. Surface stabilizes ceria in unexpected stoichiometry. *J. Phys. Chem. C* **2017**, *121* (12), 6844–6851.
- (157) Kehoe, A. B.; Scanlon, D. O.; Watson, G. W. Role of lattice distortions in the oxygen storage capacity of divalently doped CeO₂. *Chem. Mater.* **2011**, *23* (20), 4464–4468.
- (158) Nolan, M. Charge compensation and Ce³⁺ formation in trivalent doping of the CeO₂(110) surface: the key role of dopant ionic radius. *J. Phys. Chem. C* **2011**, *115* (14), 6671–6681.
- (159) Kullgren, J.; Wolf, M. J.; Castleton, C.; Mitev, P.; Briels, W. J.; Hermansson, K. Oxygen vacancies versus fluorine at CeO₂(111): A case of mistaken identity? *Phys. Rev. Lett.* **2014**, *112* (15), 156102.
- (160) Wu, X.-P.; Gong, X.-Q. Clustering of oxygen vacancies at CeO₂(111): critical role of hydroxyls. *Phys. Rev. Lett.* **2016**, *116* (8), 086102.
- (161) Walsh, A.; Sokol, A. A.; Catlow, C. R. A. Free energy of defect formation: Thermodynamics of anion Frenkel pairs in indium oxide. *Phys. Rev. B* **2011**, *83* (22), 224105.
- (162) Zhang, X.; Fu, C.; Xia, Y.; Duan, Y.; Li, Y.; Wang, Z.; Jiang, Y.; Li, H. Atomistic Origin of the Complex Morphological Evolution of Aluminum Nanoparticles during Oxidation: A Chain-like Oxide Nucleation and Growth Mechanism. *ACS Nano* **2019**, *13* (3), 3005–3014.
- (163) Mora-Fonz, D.; Lazauskas, T.; Farrow, M. R.; Catlow, C. R. A.; Woodley, S. M.; Sokol, A. A. Why are polar surfaces of ZnO stable? *Chem. Mater.* **2017**, *29* (12), 5306–5320.
- (164) Zhang, X.; Zheng, P.; Ma, Y.; Jiang, Y.; Li, H. Atomic-scale understanding of oxidation mechanisms of materials by computational approaches: A review. *Materials & Design* **2022**, *217*, 110605.